J|A|C|S ARTICLES

Published on Web 12/23/2008

Tuning the Oxidation Level, the Spin State, and the Degree of Electron Delocalization in Homo- and Heteroleptic Bis(α-diimine)iron Complexes

Marat M. Khusniyarov,* Thomas Weyhermüller, Eckhard Bill, and Karl Wieghardt*

Max-Planck-Institut für Bioanorganische Chemie, Stiftstrasse 34-36, 45470 Mülheim an der Ruhr, Germany

Received October 16, 2008; E-mail: marik@mpi-muelheim.mpg.de; wieghardt@mpi-muelheim.mpg.de

Abstract: The four-coordinate heteroleptic complex $[Fe^{III}(^{F}pda^{2-})(^{F}dad^{\bullet-})]$ (**1**) and its homoleptic analogue $[Fe^{II}(^{F}dad^{\bullet-})_2]$ (**2**), where $^{F}pda^{2-}$ is the closed-shell ligand *N,N′*-bis(pentafluorophenyl)-*o*-phenylenediamide(2−) and $^{F}dad^{\bullet-}$ is the singly reduced *N,N′*-bis(pentafluorophenyl)-2,3-dimethyl-1,4-diazabutadiene π-radical anion, have been synthesized. X-ray crystallographic studies reveal a twisted tetrahedral geometry of the FeN_4 coordination polyhedron in both **1** and **2**. The electronic structures of **1** and **2** were probed by magnetic susceptibility measurements, ^{57}Fe Mössbauer and electronic spectroscopy, and density functional theory (DFT) calculations. In spite of their similar geometries and a common triplet ground state ($S_t = 1$), the electronic structures of **1**, **2**, and the previously reported homoleptic analogue $[Fe^{III}(^{F}pda^{2-})(^{F}pda^{\bullet-})]$ (**3**), where $^{F}pda^{\bullet-}$ is a one-electron-oxidized form of $^{F}pda^{2-}$, differ. The electronic structure of **2** consists of two $^{F}dad^{\bullet-}$ radicals coupled antiferromagnetically to a high-spin Fe^{II} center, whereas in **3**, only one $^{F}pda^{\bullet-}$ radical is coupled antiferromagnetically to an intermediate-spin Fe^{III} ion. This ligand mixed-valent species exhibits class-III behavior. Heteroleptic **1** contains a single $^{F}dad^{\bullet-}$ radical coupled antiferromagnetically to an intermediate-spin Fe^{III} center but behaves as a class-II ligand mixed-valent species. The observed diversity in the electronic structures of **1**−**3** is ascribed to the difference in the redox potentials of the ligands. Analysis of reduced orbital charges and spin densities obtained from DFT calculations also suggests that the electronic structures of **1**−**3** are best described as either a high-spin Fe^{II} ion coordinated to two radical monoanions (**2**) or as an intermediate-spin Fe^{III} ion coordinated to one radical monoanion and one closed-shell dianion (**1**, **3**).

1. Introduction

1,4-Diaza-1,3-butadiene (dad) and doubly deprotonated *o*-phenylenediamine (pda) are well-known N-donor chelating ligands that form five-membered chelate rings with a large number of transition and main-group metal ions.[1] Both ligand systems are redox-active (*noninnocent*):[2] in recent years it has been clearly established that dad and pda ligands exist in three different redox forms[3] in coordination compounds, namely, (1) a closed-shell dianion, (2) an open-shell π-radical monoanion ($S_R = {}^1/_2$), and (3) a closed-shell neutral form (Chart 1).[4−17] In principle, the oxidation level of the ligands in complexes can be determined by high-quality X-ray crystallography performed at low temperatures, a broad set of spectroscopic methods, and state-of-the-art density functional theory (DFT) calculations.[4−17]

Chart 1. Oxidation Levels of pda and dad Ligands and Their Characteristic Bond Patterns (Bond Distances in Å Are Shown in Red)

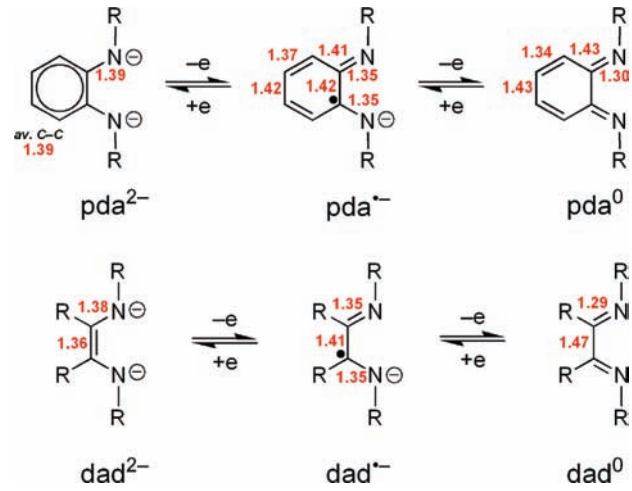

The determination of the physical oxidation state of the transition-metal ion in a complex featuring at least one redox-

(1) (a) van Koten, G.; Vrieze, K. *Adv. Organomet. Chem.* **1982**, *21*, 151. (b) Mederos, A.; Dominguez, S.; Hernandez-Molina, R.; Sanchiz, J.; Brito, F. *Coord. Chem. Rev.* **1999**, *193*−*195*, 913.

(2) (a) Büttner, T.; Geier, J.; Frison, G.; Harmer, J.; Calle, C.; Schweiger, A.; Schönberg, H.; Grützmacher, H. *Science* **2005**, *307*, 235. (b) Kaim, W. *Coord. Chem. Rev.* **1987**, *76*, 187. (c) Pierpont, C. G. *Coord. Chem. Rev.* **2001**, *216*−*217*, 99. (d) Ward, M. D.; McCleverty, J. A. *J. Chem. Soc., Dalton Trans.* **2002**, 275. (e) Vlcek, A. *Coord. Chem. Rev.* **2002**, *230*, 225. (f) Ray, K.; Petrenko, T.; Wieghardt, K.; Neese, F. *Dalton Trans.* **2007**, 1552. (g) Lever, A. B. P.; Gorelsky, S. I. *Struct. Bonding (Berlin)* **2004**, *107*, 77. (h) Kaim, W.; Schwederski, B. *Pure Appl. Chem.* **2004**, *76*, 351. (i) Chaudhuri, P.; Wieghardt, K. *Prog. Inorg. Chem.* **2001**, *50*, 151. (j) Pierpont, C. G. *Coord. Chem. Rev.* **2001**, *219*−*221*, 415. (k) Gorelsky, S. I.; Lever, A. B. P.; Ebadi, M. *Coord. Chem. Rev.* **2002**, *230*, 97.

(3) We use the general abbreviations "dad" and "pda" when the ligand oxidation level is not specified and "pda^n" and "dad^n" ($n = 0, -1, -2$) when the oxidation level is specified.

10.1021/ja808149k CCC: $40.75 © 2009 American Chemical Society

Chart 2. The Three Possible Electronic Structures of a $[Fe(dad)]^+$ Cation

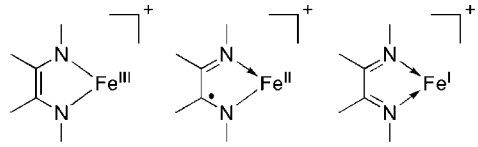

$[Fe^{III}(dad^{2-})]^+$ $[Fe^{II}(dad^{\bullet-})]^+$ $[Fe^{I}(dad^{0})]^+$

active ligand is not straightforward. For instance, monocationic $[Fe(dad)]^+$ (Chart 2) can be formulated as either (1) an Fe^{III} species with a closed-shell dianion (dad^{2-}), (2) an Fe^{II} complex with a monoanionic π-radical ligand ($dad^{\bullet-}$), or (3) an Fe^{I} species with a closed-shell neutral ligand (dad^0). In addition, we note that a ferric ion in such species may in principle adopt a high-, intermediate-, or low-spin intrinsic electron configuration ($S_{Fe} = {}^5/_2$, ${}^3/_2$, or ${}^1/_2$, respectively), and correspondingly, a ferrous ion may also be high-, intermediate-, or low-spin-configured ($S_{Fe} = 2$, 1, or 0, respectively). Strong intramolecular antiferromagnetic coupling of a π-radical monoanion ligand may then yield a large variety of different spin ground states (S_t).

During the past decade, many homoleptic transition-metal complexes containing either pda[6−10] or dad[13−17] ligands were synthesized, and the electronic structures of a few of these species were thoroughly investigated. However, *heteroleptic* complexes containing both a pda ligand and a dad ligand have not been reported to date. Since both pda and dad are members of the same α-diimine family, they display considerable similarities in their donor−acceptor abilities, which renders the formation and isolation of heteroleptic complexes [M(pda)(dad)] difficult. The redox potentials of given pda and dad ligands are expected to be different, and a heteroleptic complex [M(pda)(dad)] is expected to possess electronic properties that differ from those of the parent homoleptic complexes $[M(pda)_2]$ and $[M(dad)_2]$.

Chart 3. Ligands and Complexes Used in This Work

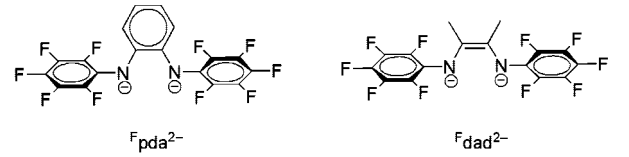

^{F}pda^{2-} ^{F}dad^{2-}

$[Fe^{III}(^Fpda^{2-})(^Fdad^{\bullet-})]$	$[Fe^{II}(^Fdad^{\bullet-})_2]$	$[Fe^{III}(^Fpda^{2-})(^Fpda^{\bullet-})]$
1	**2**	**3**
$S_{Fe} = 3/2$; $S_t = 1$	$S_{Fe} = 2$; $S_t = 1$	$S_{Fe} = 3/2$; $S_t = 1$
Class II		Class III
Mössbauer parameters at 80K:		
$\delta = 0.33$ mm s^{-1}	$\delta = 0.54$ mm s^{-1}	$\delta = 0.23$ mm s^{-1}
$\lvert\Delta E_Q\rvert = 4.46$ mm s^{-1}	$\lvert\Delta E_Q\rvert = 4.96$ mm s^{-1}	$\lvert\Delta E_Q\rvert = 4.45$ mm s^{-1}

Here we report the synthesis, spectroscopic investigation, and DFT calculations on the first heteroleptic complex [Fe(^{F}pda)(^{F}dad)] (**1**), where ^{F}pda is *N*,*N*′-bis(pentafluorophenyl)-*o*-phenylenediamide and ^{F}dad is *N*,*N*′-bis(pentafluorophenyl)-2,3-dimethyl-1,4-diaza-1,3-butadiene (Chart 3). Since **1** contains three different redox centers, the assignment of oxidation and spin states within the complex is particularly difficult. In order to understand the electronic structure of **1**, we also prepared the homoleptic complex [Fe(^{F}dad)$_2$] (**2**). The homoleptic counterpart, namely, the complex [Fe(^{F}pda)$_2$] (**3**), has been reported recently (Chart 3).[18] As we will show, intramolecular $\pi-\pi$ stacking between the *N*-C_6F_5 substituents causes complexes **1**−**3** to adopt very similar twisted geometries of the FeN_4 polyhedron that are intermediate between square-planar and tetrahedral, but similar geometries do not necessarily lead to similar electronic structures. Despite the fact that complexes **1**, **2**, and **3** all possess an $S_t = 1$ ground state, they display very different spectroscopic properties (electronic and Mössbauer spectra), indicating that the common triplet ground state is composed quite differently (Chart 3). The origin of this difference is thought to be a consequence of the differing redox potentials ($E^1_{1/2} \neq E^2_{1/2}$, eqs 1 and 2):

$$^F\text{pda}^{2-} \underset{+e}{\overset{-e}{\rightleftarrows}} {}^F\text{pda}^{\bullet-} \quad (E_{redox} = E^1_{1/2}) \tag{1}$$

$$^F\text{dad}^{2-} \underset{+e}{\overset{-e}{\rightleftarrows}} {}^F\text{dad}^{\bullet-} \quad (E_{redox} = E^2_{1/2}) \tag{2}$$

The gross influence of the ligand redox potentials on the electronic structures of **1**−**3** is investigated. The computational

(4) Carugo, O.; Djinovic, K.; Rizzi, M.; Castellani, C. B. *J. Chem. Soc., Dalton Trans.* **1991**, 1551.
(5) Metcalfe, R. A.; Lever, A. B. P. *Inorg. Chem.* **1997**, *36*, 4762.
(6) (a) Ghosh, P.; Begum, A.; Herebian, D.; Bothe, E.; Hildenbrand, K.; Weyhermüller, T.; Wieghardt, K. *Angew. Chem., Int. Ed.* **2003**, *42*, 563. (b) Bill, E.; Bothe, E.; Chaudhuri, P.; Chlopek, K.; Herebian, D.; Kokatam, S.; Ray, K.; Weyhermüller, T.; Neese, F.; Wieghardt, K. *Chem.—Eur. J.* **2005**, *11*, 204. (c) Maji, S.; Patra, S.; Chakraborty, S.; Janardanan, D.; Mobin, S. M.; Sunoj, R. B.; Lahiri, G. K. *Eur. J. Inorg. Chem.* **2007**, 314.
(7) Herebian, D.; Bothe, E.; Neese, F.; Weyhermüller, T.; Wieghardt, K. *J. Am. Chem. Soc.* **2003**, *125*, 9116.
(8) Chlopek, K.; Bill, E.; Weyhermüller, T.; Wieghardt, K. *Inorg. Chem.* **2005**, *44*, 7087.
(9) (a) Rusanova, J.; Rusanov, E.; Gorelsky, S. I.; Christendat, D.; Popescu, R.; Farah, A. A.; Beaulac, R.; Reber, C.; Lever, A. B. P. *Inorg. Chem.* **2006**, *45*, 6246. (b) Ketterer, N. A.; Fan, H.; Blackmore, K. J.; Yang, X.; Ziller, J. W.; Baik, M.-H.; Heyduk, A. F. *J. Am. Chem. Soc.* **2008**, *130*, 4364.
(10) Khusniyarov, M. M.; Harms, K.; Burghaus, O.; Sundermeyer, J.; Sarkar, B.; Kaim, W.; van Slageren, J.; Duboc, C.; Fiedler, J. *Dalton Trans.* **2008**, 1355.
(11) (a) Kaim, W.; Matheis, W. *J. Chem. Soc., Chem. Commun.* **1991**, 597. (b) Kaupp, M.; Stoll, H.; Preuss, H.; Kaim, W.; Stahl, T.; Van Koten, G.; Wissing, E.; Smeets, W. J. J.; Spek, A. L. *J. Am. Chem. Soc.* **1991**, *113*, 5606. (c) Lorenz, V.; Thiele, K. H.; Neumüller, B. *Z. Anorg. Allg. Chem.* **1994**, *620*, 691.
(12) Gardiner, M. G.; Hanson, G. R.; Henderson, M. J.; Lee, F. C.; Raston, C. L. *Inorg. Chem.* **1994**, *33*, 2456.
(13) (a) Rijnberg, E.; Richter, B.; Thiele, K.-H.; Boersma, J.; Veldman, N.; Spek, A. L.; van Koten, G. *Inorg. Chem.* **1998**, *37*, 56. (b) Pott, T.; Jutzi, P.; Kaim, W.; Schoeller, W. W.; Neumann, B.; Stammler, A.; Stammler, H.-G.; Wanner, M. *Organometallics* **2002**, *21*, 3169.
(14) (a) Tuononen, H. M.; Armstrong, A. F. *Inorg. Chem.* **2005**, *44*, 8277. (b) Tuononen, H. M.; Armstrong, A. F. *Dalton Trans.* **2006**, 1885. (c) Bailey, P. J.; Dick, C. M.; Fabre, S.; Parsons, S.; Yellowlees, L. J. *Dalton Trans.* **2006**, 1602. (d) Ghosh, M.; Weyhermüller, T.; Wieghardt, K. *Dalton Trans.* **2008**, 5149.
(15) Khusniyarov, M. M.; Harms, K.; Burghaus, O.; Sundermeyer, J. *Eur. J. Inorg. Chem.* **2006**, 2985.
(16) (a) Muresan, N.; Chlopek, K.; Weyhermüller, T.; Neese, F.; Wieghardt, K. *Inorg. Chem.* **2007**, *46*, 5327. (b) Muresan, N.; Weyhermüller, T.; Wieghardt, K. *Dalton Trans.* **2007**, 4390. (c) Ghosh, M.; Sproules, S.; Weyhermüller, T.; Wieghardt, K. *Inorg. Chem.* **2008**, *47*, 5963.
(17) Muresan, N.; Lu, C. C.; Ghosh, M.; Peters, J. C.; Abe, M.; Henling, L. M.; Weyhermüller, T.; Bill, E.; Wieghardt, K. *Inorg. Chem.* **2008**, *47*, 4579.
(18) Khusniyarov, M. M.; Bill, E.; Weyhermüller, T.; Bothe, E.; Harms, K.; Sundermeyer, J.; Wieghardt, K. *Chem.—Eur. J.* **2008**, *14*, 7608.

analysis of reduced orbital charges and spin densities[19] discloses sophisticated electronic structures of **1**−**3**.

2. Experimental Section

a. Syntheses. The starting materials [Fe(^{F}pda)(dme)$_2$] (dme = dimethoxyethane)[20] and ^{F}dad[15] were prepared according to reported procedures. All of the syntheses were performed under a dry, oxygen-free argon atmosphere using standard Schlenk techniques and dried solvents.

[Fe(^{F}pda)(^{F}dad)] (1). A solution of ^{F}dad (184 mg, 0.442 mmol) in toluene (10 mL) was slowly added to [Fe(^{F}pda)(dme)$_2$][20] (296 mg, 0.439 mmol) dissolved in toluene (10 mL) and cooled to −80 °C. The reaction mixture was stirred at room temperature for 30 min. After the solution was decanted via cannula, the dark-green solid obtained was dried in vacuo. Crystals suitable for single-crystal X-ray diffractometry were obtained from a toluene solution on cooling. Yield: 367 mg (92%). Anal. Calcd for $C_{34}H_{10}F_{20}FeN_4$: C, 44.86; H, 1.11; N, 6.15. Found: C, 44.86; H, 0.95; N, 6.07.

[Fe(^{F}dad)$_2$] (2). Anhydrous $FeCl_2$ (63 mg, 0.497 mmol), ^{F}dad (416 mg, 1.000 mmol) and sodium (24 mg, 1.043 mmol) were combined into one Schlenk flask, and Et_2O (20 mL) was added. After the flask was sonicated in an ultrasonic bath for 30 min, the reaction mixture was stirred at room temperature for ∼2 days. The solvent was evaporated in vacuo, and the green crude product was recrystallized from a 5:7 hexane/Et_2O mixture by cooling. Crystals suitable for single-crystal X-ray diffractometry were obtained from a saturated toluene solution on cooling. Yield: 176 mg (40%). Anal. Calcd for $C_{32}H_{11}F_{20}FeN_4$: C, 43.27; H, 1.36; N, 6.31. Found: C, 43.97; H, 1.47; N, 6.53.

b. Physical Measurements. Electronic spectra were recorded with a PerkinElmer Lambda 19 double-beam UV−vis−NIR spectrometer (300−2000 nm). The program PeakFit version 4.06 was used to deconvolute the electronic spectra. Temperature-dependent magnetic susceptibility data were recorded on an MPMS Quantum Design SQUID magnetometer in the temperature range 2−300 K. The experimental magnetic susceptibility data were corrected for underlying diamagnetism and temperature-independent paramagnetism. Mössbauer data were recorded on alternating constant-acceleration spectrometers. The sample temperature was held constant in an Oxford Instruments Variox cryostat or an Oxford Instruments Mössbauer-Spectromag cryostat. The latter was used for measurement in applied magnetic fields with the field oriented perpendicular to the γ-beam. Isomer shifts are given relative to α-Fe at room temperature. Elemental analyses were performed by the Microanalytical Laboratory, Mr. Kolbe, Mülheim an der Ruhr, Germany.

c. X-ray Crystallographic Data Collection and Refinement of Structures. Black single crystals of **1** and **2** were coated with perfluoropolyether, picked up with nylon loops and mounted in the nitrogen cold stream of a Bruker APEX2 diffractometer equipped with a Mo-target rotating-anode X-ray source and INCOTEC Mo-Multi-Layer-Optics. Graphite-monochromatized Mo Kα radiation (λ = 0.71073 Å) was used throughout. Final cell constants were obtained from least-squares fits of several thousand strong reflections. Intensity data were corrected for absorption using intensities of redundant reflections. The structures were readily solved by Patterson methods and subsequent difference Fourier techniques. The Siemens ShelXTL[21] software package was used for solution and artwork of the structures, and ShelXL97[22] was used for the refinement. All of the non-hydrogen atoms were anisotropically refined, and hydrogen atoms were placed at calculated positions and refined as riding atoms with isotropic displacement parameters. Crystallographic data are listed in Table 1.

Table 1. Crystallographic Data for **1** and **2**

	1·C_7H_8	**2**·C_7H_8
chemical formula	$C_{41}H_{18}F_{20}FeN_4$	$C_{39}H_{20}F_{20}FeN_4$
formula weight	1002.44	980.44
crystal size (mm)	0.06 × 0.05 × 0.02	0.04 × 0.01 × 0.01
crystal system	orthorhombic	orthorhombic
space group	*Pbcn* (No. 60)	*Pbcn* (No. 60
a (Å)	20.0711(10)	20.008(4)
b (Å)	13.0077(6)	13.025(3)
c (Å)	13.9583(7)	14.096(3)
V (Å^3)	3644.2(3)	3673.5(14)
Z	4	4
T, K	100(2)	100(2)
ρ_{calcd} (g cm^{-3})	1.827	1.773
refl. collected, $2\Theta_{max}$	293573, 60.00	50354, 50.00
unique refl., $I > 2\sigma(I)$	5308, 3932	3238, 2308
params, restraints	331, 0	308, 0
λ (Å), μ(Kα) (cm^{-1})	0.71073, 5.58	0.71073, 5.51
R1[a], goodness of fit[b]	0.0416, 1.186	0.0364, 1.059
wR2[c] [$I > 2\sigma(I)$]	0.0904	0.0825
residual density, eÅ^{-3}	+0.43, −0.51	+0.47, −0.39

[a] Observation criterion: $I > 2\sigma(I)$. R1 = $\sum||F_o| - |F_c||/\sum|F_o|$. [b] GOF = $[\sum w(F_o^2 - F_c^2)^2/(n - p)]^{1/2}$. [c] wR2 = $[\sum w(F_o^2 - F_c^2)^2/\sum w(F_o^2)^2]^{1/2}$, where $w = 1/\sigma^2(F_o^2) + (aP)^2 + bP$, $P = (F_o^2 + 2F_c^2)/3$.

Ligand positions in complex **1** were found to be interchanged due to their similar space requirement. The molecule lies on a crystallographic twofold axis that runs through the ligands and the metal. A split-atom model was set up for the atoms concerned. Nitrogen atoms, pentafluorophenyl rings, and carbon atoms C8 and C18 were left unsplit since the metrical parameters of the two ligands are very similar with respect to the Ph−N−C−C−N−Ph unit. The split positions for carbon atoms C9, C10 and C19, C20 were derived from the difference map and were anisotopically refined with equal displacement parameters for corresponding atoms using the EADP instruction of ShelXL97. The occupation ratio in this model refined to a value of ∼0.61:0.39.

A toluene molecule of crystallization was found to be disordered on a crystallographic inversion center in both structures. The ring geometry was fixed to retain a perfect hexagon, and an occupation factor of 0.5 was used for the refinement of its position. The carbon position of the methyl group was easily derived from the difference map and was refined without further restraints.

d. Calculations. The program package ORCA 2.6 revision 35 was used for all of the calculations.[23] Spin-unrestricted DFT calculations for all of the complexes in this work were performed on the X-ray structures, where only hydrogen atoms were optimized with the B3LYP functional.[24] The ligands were all-atoms-optimized with the B3LYP functional; the N−C−C−N torsion angle in ^{F}dad^0 was fixed at 0°, providing a cis form, and the corresponding N−C−C−N angle in ^{F}pda^0 was fixed at 0° for consistency. Convergence criteria for geometry optimization were set to default values (OPT), and "tight" convergence criteria were used for SCF calculations (TIGHTSCF). Triple-ζ basis sets with one set of polarization functions[25] (TZVP) were used for the iron and nitrogen atoms, and double-ζ basis sets with one set of polarization functions[26] (SVP) were used for all of the other atoms. The

(19) *Manual for ORCA, version 2.6, revision 35*; Institut für Physikalische und Theoretische Chemie, Universität Bonn: Bonn, Germany, 2007; p 296.
(20) Khusniyarov, M. M.; Weyhermüller, T.; Bill, E.; Wieghardt, K. *Angew. Chem., Int. Ed.* **2008**, *47*, 1228.
(21) *ShelXTL*, version 6.14; Bruker AXS Inc.: Madison, WI, 2003.
(22) Sheldrick, G. M. *ShelXL97*; University of Göttingen: Göttingen, Germany, 1997.
(23) Neese, F. *ORCA: An Ab Initio, Density Functional and Semiempirical Program Package*, version 2.6, revision 35; Institut für Physikalische und Theoretische Chemie, Universität Bonn: Bonn, Germany, July 2007.
(24) (a) Becke, A. D. *J. Chem. Phys.* **1993**, *98*, 5648. (b) Lee, C. T.; Yang, W. T.; Parr, R. G. *Phys. Rev. B* **1988**, *37*, 785. (c) Stephens, P. J.; Devlin, F. J.; Chabalowski, C. F.; Frisch, M. J. *J. Phys. Chem.* **1994**, *98*, 11623.
(25) Schafer, A.; Huber, C.; Ahlrichs, R. *J. Chem. Phys.* **1994**, *100*, 5829.
(26) Schafer, A.; Horn, H.; Ahlrichs, R. *J. Chem. Phys.* **1992**, *97*, 2571.

resolution of the identity approximation (RIJONX) was employed[27,28] with matching auxiliary basis sets.[28] Electronic energies and properties were calculated using the B3LYP functional with the same basis sets and SCF convergence criteria as for the geometry optimizations. Broken-symmetry (BS) solutions[29,30] were analyzed via the corresponding orbital transformation.[31] For the calculation of Mössbauer parameters, the "core" CP(PPP) basis set for iron[32] with enhanced integration accuracy on the iron (SPECIALGRID-INTACC 7) was used. High-spin states were calculated on the BS geometries when the exchange coupling constants were estimated.[33] All of the reduced orbital charges and spin densities[19] were calculated according to Löwdin population analysis.[34] Reduced orbital population is defined as a population per angular momentum type,[19] meaning the decomposition of the total spin or charge population at the given atom into the population of s, p_i, d_i and f_i orbitals of the atom. Time-dependent DFT (TD-DFT) calculations were performed using the B3LYP functional and the conductor-like screening model (COSMO)[35] with hexane as a solvent. The first 20 states were calculated, where the maximum dimension of the expansion space in the Davidson procedure (MAXDIM) was set to 200. Molecular orbitals (MOs) and spin densities were visualized via the program Molekel.[36]

3. Results

a. Synthesis and Crystal Structures. Reaction of 3 equiv of ^{F}dad with 2 equiv of [Fe(^{F}pda)(dme)$_2$] led unexpectedly to the isolation of the heteroleptic complex **1** (Chart 3). No evidence for the formation of the coordination salt [Fe(^{F}dad)$_3$][Fe(^{F}pda)$_2$] was observed.[20] The purity and yield of **1** improved when equimolar amounts of the reagents were used. The homoleptic complex **2** was prepared by reduction of the ^{F}dad ligand with elemental sodium in the presence of anhydrous iron dichloride.[17,37,38] In our experience, this type of reaction proceeds very slowly in nonpolar solvents but is faster in polar solvents. Therefore, the use of polar solvents such as diethyl ether is advisable. Both complexes **1** and **2** are very air- and water-sensitive.

Table 2. Selected Bond Lengths (Å) and Twist Angle α (deg) in **1**−**3**

	1	2	3[a]
Fe1−N1	1.912(2)	1.962(2)	1.898(2)
Fe1−N11	1.920(2)	1.962(2)	1.897(2)
N1−C8	1.366(3)	1.359(4)	1.380(4)
N11−C18	1.361(3)	1.361(4)	1.384(4)
C18−C18#	1.412(5)	1.400(7)	1.422(4)
C8−C8#	1.412(4)	1.400(6)	1.426(4)
C9−C10	1.37(3)		1.373(4)
C10−C10#	1.390(9)		1.406(4)
C8−C9	1.40(3)		1.405(4)
α[b]	51.3	58.7	54.0

[a] Data are from ref 18; the average values are given. [b] The dihedral angle between the C_2N_2Fe and C_6N_2Fe planes.

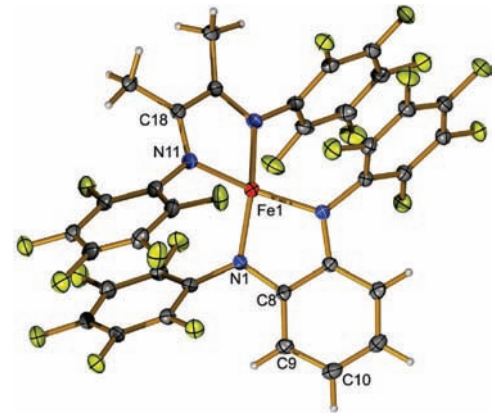

Figure 1. Molecular structure of **1** (site symmetry C_2), with thermal ellipsoids drawn at the 40% probability level. Color scheme: red, Fe; yellow, F; blue, N; gray, C.

The heteroleptic complex **1** crystallizes in the orthorhombic crystal system (space group *Pbcn*). Four molecules of **1** (Z = 4) and two molecules of toluene are present in the unit cell. Selected bond distances and angles are summarized in Table 2. Both of the chelating ligands ^{F}pda and ^{F}dad are coordinated to the central iron ion, forming a twisted tetrahedral geometry in which the two ligand planes form a dihedral angle (α) of 51.3° (Figure 1 and Figure S1 in the Supporting Information). The two pairs of C_6F_5 substituents show the presence of intramolecular π−π interactions, which are responsible for the formation of the twisted geometry as discussed previously.[10,15] The short Fe−N bond distances of 1.912−1.920(2) Å rule out a description of the central iron as a high-spin Fe^{II} ion (Table 2). The geometric pattern of the ^{F}dad backbone, with two relatively long C−N bonds [1.361(3) Å] and a C−C bond length of 1.412(5) Å, points to the presence of an open-shell π-radical ligand ^{F}dad$^{\bullet-}$ (Chart 1).[12,13,15−17,39] Because of the observed static disorder in the crystal structure of **1**, the standard deviations of the bond distances within the ^{F}pda ligand are too large to allow the unambiguous determination of the oxidation level of this ligand. However, the relatively long C−N bond distances of 1.366(3)

(27) (a) Baerends, E. J.; Ellis, D. E.; Ros, P. *Chem. Phys.* **1973**, *2*, 41. (b) Dunlap, B. I.; Connolly, J. W. D.; Sabin, J. R. *J. Chem. Phys.* **1979**, *71*, 3396. (c) Vahtras, O.; Almlof, J.; Feyereisen, M. W. *Chem. Phys. Lett.* **1993**, *213*, 514.
(28) (a) Eichkorn, K.; Treutler, O.; Ohm, H.; Haser, M.; Ahlrichs, R. *Chem. Phys. Lett.* **1995**, *242*, 652. (b) Eichkorn, K.; Weigend, F.; Treutler, O.; Ahlrichs, R. *Theor. Chem. Acc.* **1997**, *97*, 119.
(29) (a) Adamo, C.; Barone, V.; Bencini, A.; Totti, F.; Ciofini, I. *Inorg. Chem.* **1999**, *38*, 1996. (b) Ginsberg, A. P. *J. Am. Chem. Soc.* **1980**, *102*, 111. (c) Noodleman, L. *J. Chem. Phys.* **1981**, *74*, 5737. (d) Noodleman, L.; Norman, J. G.; Osborne, J. H.; Aizman, A.; Case, D. A. *J. Am. Chem. Soc.* **1985**, *107*, 3418. (e) Noodleman, L.; Davidson, E. R. *Chem. Phys.* **1986**, *109*, 131. (f) Noodleman, L.; Case, D. A.; Aizman, A. *J. Am. Chem. Soc.* **1988**, *110*, 1001. (g) Noodleman, L.; Peng, C. Y.; Case, D. A.; Mouesca, J. M. *Coord. Chem. Rev.* **1995**, *144*, 199. (h) Ovchinnikov, A. A.; Labanowski, J. K. *Phys. Rev. A* **1996**, *53*, 3946. (i) Bachler, V.; Olbrich, G.; Neese, F.; Wieghardt, K. *Inorg. Chem.* **2002**, *41*, 4179.
(30) Herebian, D.; Wieghardt, K. E.; Neese, F. *J. Am. Chem. Soc.* **2003**, *125*, 10997.
(31) (a) Amos, A. T.; Hall, G. G. *Proc. R. Soc. London, Ser. A* **1961**, *263*, 483. (b) King, H. F.; Stanton, R. E.; Kim, H.; Wyatt, R. E.; Parr, R. G. *J. Chem. Phys.* **1967**, *47*, 1936. (c) Neese, F. *J. Phys. Chem. Solids* **2004**, *65*, 781.
(32) (a) Neese, F. *Inorg. Chim. Acta* **2002**, *337*, 181. (b) Sinnecker, S.; Slep, L. D.; Bill, E.; Neese, F. *Inorg. Chem.* **2005**, *44*, 2245.
(33) (a) Soda, T.; Kitagawa, Y.; Onishi, T.; Takano, Y.; Shigeta, Y.; Nagao, H.; Yoshioka, Y.; Yamaguchi, K. *Chem. Phys. Lett.* **2000**, *319*, 223. (b) Yamaguchi, K.; Takahara, Y.; Fueno, T. In *Applied Quantum Chemistry*; Smith, V. H., Ed.; Reidel: Dordrecht, The Netherlands, 1986; p 155.
(34) (a) Löwdin, P. O. *J. Chem. Phys.* **1950**, *18*, 365. (b) Löwdin, P. O. *Adv. Quantum Chem.* **1970**, *5*, 185.
(35) Klamt, A.; Schuurmann, G. *J. Chem. Soc., Perkin Trans. 2* **1993**, 799.
(36) Portmann, S. *Molekel*, version 4.3.win32; CSCS/UNI Geneva: Geneva, Switzerland, 2002.
(37) Bart, S. C.; Hawrelak, E. J.; Lobkovsky, E.; Chirik, P. J. *Organometallics* **2005**, *24*, 5518.
(38) (a) tom Dieck, H.; Bruder, H. *J. Chem. Soc., Chem. Commun.* **1977**, 24. (b) tom Dieck, H.; Diercks, R.; Stamp, L.; Bruder, H.; Schuld, T. *Chem. Ber.* **1987**, *120*, 1943.
(39) (a) Moore, J. A.; Cowley, A. H.; Gordon, J. C. *Organometallics* **2006**, *25*, 5207. (b) Kreisel, K. A.; Yap, G. P. A.; Theopold, K. H. *Inorg. Chem.* **2008**, *47*, 5293.

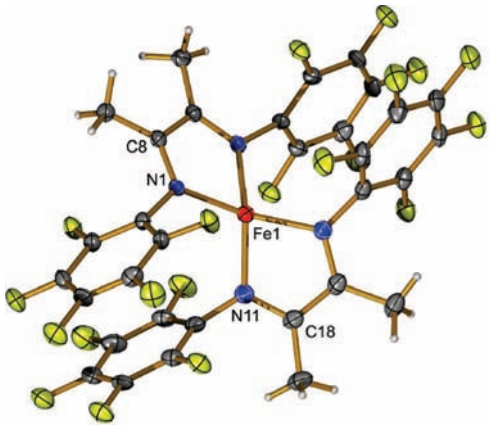

Figure 2. Molecular structure of **2** (site symmetry C_2), with thermal ellipsoids drawn at the 40% probability level. Color scheme: red, Fe; yellow, F; blue, N; gray, C.

Å within the coordinated ^{F}pda ligand may point to a radical character of the ligand (^{F}pda$^{\bullet-}$).[4,6−8,10,40]

The structure of the neutral homoleptic complex **2** is similar to that of **1**. The twist angle $\alpha = 58.7°$ formed by the two ^{F}dad ligand planes in **2** is slightly larger than that in **1** (Figure 2). Again, the two pairs of C_6F_5 substituents involved in intramolecular $\pi-\pi$ interactions are responsible for the formation of the twisted geometry of **2**. Relatively short C−C bonds [1.400(7) and 1.400(6) Å] in comparison with the neutral form of the ligand and relatively long C−N bonds [1.361(4) and 1.359(4) Å] within ^{F}dad backbone prove that both ligands in **2** are monoanionic π-radical ligands ^{F}dad$^{\bullet-}$. The Fe−N bond distances of 1.962(2) Å in **2** are longer than those found in intermediate-spin Fe^{III} complexes possessing a similar twisted FeN_4 geometry [1.875−1.905(5) Å].[18,20] Since the presence of two monoanionic ligands in neutral **2** requires a ferrous metal center, the electronic structure of **2** should be described as [Fe^{II}(^{F}dad$^{\bullet-}$)$_2$].

b. Magnetism. Data from variable-temperature (VT) magnetic susceptibility and variable-temperature variable-field (VTVH) magnetization measurements on **1** and **2** are shown in Figures 3 and 4, respectively. The effective magnetic moment (μ_{eff}) of 2.98−3.00μ_B measured for **1** in an applied field of 1 T is nearly temperature-independent over the temperature range 50−290 K. This is consistent with a triplet ground state ($S_t = 1$), which is the only thermally populated state at temperatures up to 290 K. At temperatures below 50 K, μ_{eff} decreases gradually with decreasing temperature as a result of zero-field splitting of the ground triplet. Two fits of similar quality for the VTVH magnetization measurements were obtained, with zero-field splitting parameter values of (1) $D_t = +15.0$ cm^{-1} and $E/D_t = 0.0$ (Figure 3) and (2) $D_t = -20.7$ cm^{-1} and $E/D_t = 0.23$ (Figure S2 in the Supporting Information). Thus, it was not possible to determine the sign of the axial zero-field splitting parameter experimentally.

Compound **2** possesses an effective magnetic moment of 2.88−2.91μ_B in the temperature range 60−290 K, which is also consistent with a triplet ground state. At low temperatures ($T < 60$ K), μ_{eff} decreases gradually as a result of zero-field splitting of the $S_t = 1$ state. According to the VTVH magnetization measurements at three different fields, the axial zero-field splitting parameter D_t is positive with a value of 17.6 cm^{-1}, and the rhombic parameter E/D_t is 0.19.

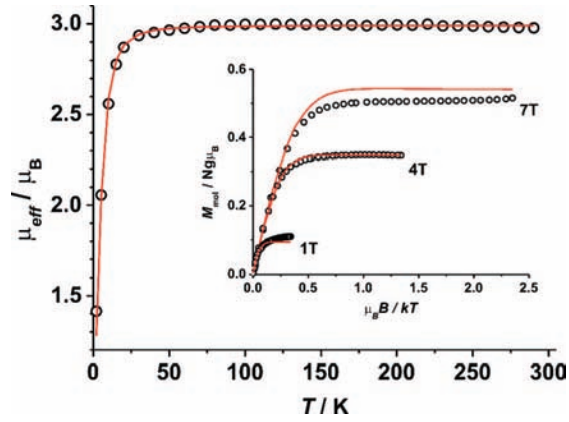

Figure 3. Temperature dependence of the effective magnetic moment of **1** recorded at 1 T. The inset shows the variable-field temperature dependence of the magnetization of **1**. The solid lines in red represent best fits obtained using $g_t = 2.12$, $D_t = 15.0$ cm^{-1}, $E/D_t = 0.0$, and $S_t = 1$. If it is assumed that $S_{Fe} = {}^3/_2$, $S_R = {}^1/_2$, and $S_t = 1$, using spin-projection techniques[57] yields a calculated value of $D_{Fe} = {}^2/_3 D_t = 10.0$ cm^{-1} for the local iron **D** tensor.

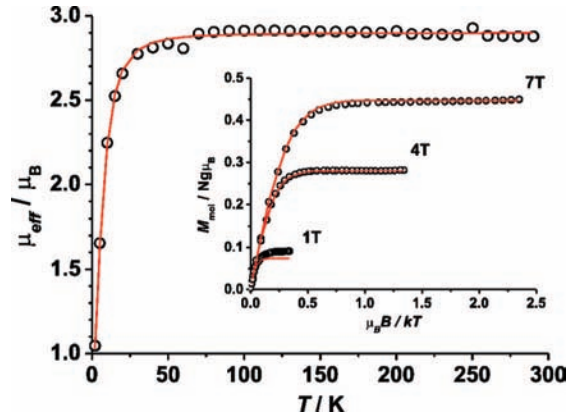

Figure 4. Temperature dependence of the effective magnetic moment of **2** recorded at 1 T. The inset shows the variable-field temperature dependence of the magnetization of **2**. The solid lines in red represent best fits obtained using $g_t = 2.05$, $D_t = 17.6$ cm^{-1}, and $E/D_t = 0.19$. If it is assumed that $S_{Fe} = 2$, $S^* = S_{R1} + S_{R2} = 1$, and $S_t = 1$, using spin-projection techniques[57] yields a calculated value of $D_{Fe} = {}^{10}/_{21} D_t = 8.4$ cm^{-1} for the local iron **D** tensor.

c. Mössbauer Spectroscopy. The zero-field ^{57}Fe Mössbauer spectrum of a microcrystalline sample of **1** (Figure 5) reveals a quadrupole doublet with an isomer shift (δ) of 0.33 mm s^{-1} and a quadrupole splitting ($|\Delta E_Q|$) of 4.46 mm s^{-1} at 80 K and a minor doublet ($\delta = 0.39$ mm s^{-1}, $|\Delta E_Q| = 0.92$ mm s^{-1}) of an unknown impurity (9%). The relatively small isomer shift and very large quadrupole splitting are typical for four-[18,20,41] and five-coordinate[8,42,43] intermediate-spin ferric species. For example, the twisted complex [Fe^{III}(^{F}pda^{2-})(^{F}pda$^{\bullet-}$)] **3** ($S_t = 1$) with an intermediate-spin Fe^{III} center has $\delta = 0.23$ mm s^{-1} and $\Delta E_Q = +4.45$ mm s^{-1}.[18] From the fit of the applied field Mössbauer spectra of **1** (Figure 6), it is possible to

(40) Chlopek, K.; Bothe, E.; Neese, F.; Weyhermüller, T.; Wieghardt, K. *Inorg. Chem.* **2006**, *45*, 6298.

(41) Fang, M.; Wilson, S. R.; Suslick, K. S. *J. Am. Chem. Soc.* **2008**, *130*, 1134.

(42) (a) Patra, A. K.; Bill, E.; Weyhermüller, T.; Stobie, K.; Bell, Z.; Ward, M. D.; McCleverty, J. A.; Wieghardt, K. *Inorg. Chem.* **2006**, *45*, 6541. (b) Ray, K.; Bill, E.; Weyhermüller, T.; Wieghardt, K. *J. Am. Chem. Soc.* **2005**, *127*, 5641. (c) Ghosh, P.; Bill, E.; Weyhermüller, T.; Wieghardt, K. *J. Am. Chem. Soc.* **2003**, *125*, 3967. (d) Blanchard, S.; Bill, E.; Weyhermüller, T.; Wieghardt, K. *Inorg. Chem.* **2004**, *43*, 2324.

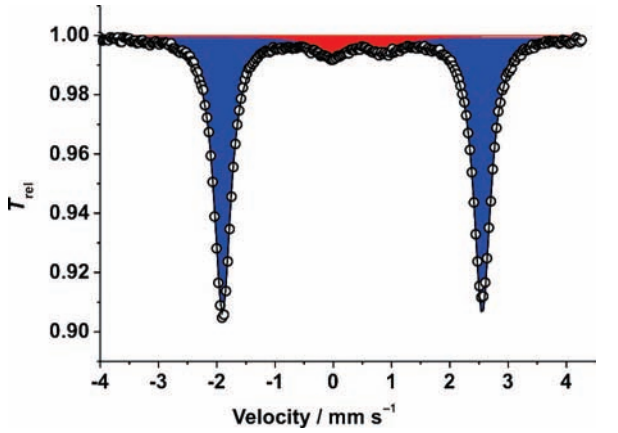

Figure 5. Zero-field ^{57}Fe Mössbauer spectrum of a powder sample of **1** recorded at 80 K. The solid line represents the best fit obtained with the following parameter values: (a) **1**, $\delta = 0.33$ mm s^{-1}, $|\Delta E_Q| = 4.46$ mm s^{-1}, relative intensity 91%; (b) an unidentified impurity, $\delta = 0.39$ mm s^{-1}, $|\Delta E_Q| = 0.92$ mm s^{-1}, relative intensity 9%. Color scheme for the quadrupole doublets: blue, **1**; red, the impurity.

determine a positive sign of the quadrupole splitting constant. The hyperfine coupling tensor **A** shows two positive components, $A_{t,xx} = A_{t,zz} = 6.6$ T, and one larger negative component, $A_{t,yy} = -15.0$ T. The principal axis system of the **A** tensor is rotated by 90° around the *y* axis of the principal axis system of the electric field gradient (EFG) tensor (Euler angle $\beta = 90°$, Figure 7). A very similar **A** tensor showing two positive components, one large negative component, and $\beta = 90°$ was observed for **3**.[18] Another possible fit of the applied field Mössbauer spectra of **1** is discussed in the Supporting Information.

The Mössbauer spectrum of **2** recorded at zero field shows a dominant quadrupole doublet with parameter values $\delta = 0.54$ mm s^{-1} and $|\Delta E_Q| = 4.96$ mm s^{-1} (Figure 8). The isomer shift and the quadrupole splitting are both larger in **2** than in **1**. The observed parameter values for **2** could indicate a central high-spin Fe^{II} ion,[17] but the situation seems to be borderline between a typical intermediate-spin ferric ion and a typical high-spin ferrous ion. For example, the high-spin Fe^{II} ion in the twisted tetrahedral dianion $[Fe^{II}(^{F}pda^{2-})_2]^{2-}$ exhibits $\delta = 0.72$ mm s^{-1} and $|\Delta E_Q| = 3.07$ mm s^{-1} or $\delta = 0.68$ mm s^{-1} and $|\Delta E_Q| = 5.20$ mm s^{-1}, depending on the twist angle (44.9 or 57.1°, respectively).[18,20]

d. Electronic Spectra. The electronic spectra of **1** and **2** are shown in Figures 9 and 10, respectively. The spectrum of **1** is dominated by a series of very intense charge-transfer bands in the visible and NIR regions. The intense band ($\varepsilon = 2.1 \times 10^3$ M^{-1} cm^{-1}) at ~1000 nm is assigned as intervalence ligand-to-ligand charge transfer (IVLLCT) band in the ligand mixed-valent

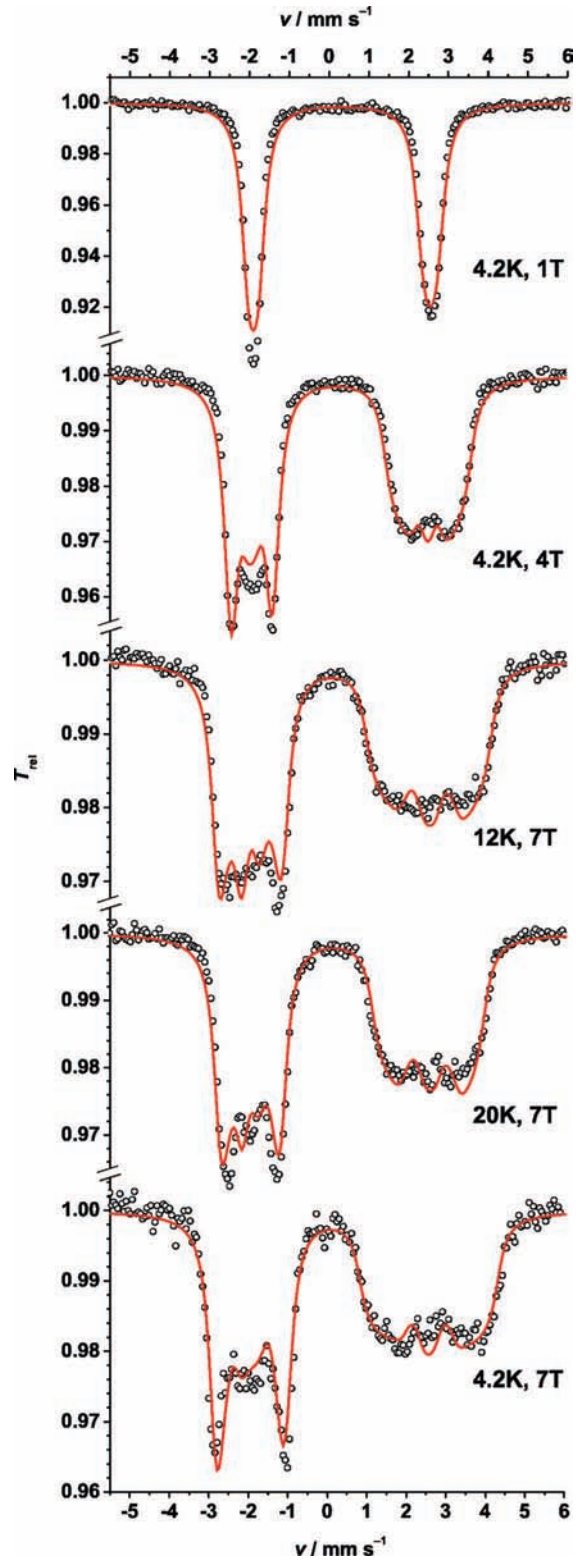

Figure 6. Applied-field ^{57}Fe Mössbauer spectra of crystalline **1** recorded at varying temperatures and varying applied fields. The solid lines in red represent the best fits obtained using the parameter values $S_t = 1$, $\delta = 0.32$ mm s^{-1}, $\Delta E_Q = +4.44$ mm s^{-1}, $\eta = 0.9$, $D_t = +15.0$ cm^{-1}, $E/D_t = 0.0$, $g_x = g_y = g_z = 2.12$, $A_{t,xx} = A_{t,zz} = 6.6$ T, $A_{t,yy} = -15.0$ T, and $\beta = 90°$. The effective (total) **D** and **A** tensors obtained for the ground triplet can be converted into the local tensors using spin-projection techniques: $D_{Fe} = {}^2/_3 D_t = 10.0$ cm^{-1}; $A_{Fe,xx} = A_{Fe,zz} = {}^4/_5 A_{t,zz} = 5.3$ T, $A_{Fe,yy} = {}^4/_5 A_{t,yy} = -12.0$ T.

(43) (a) Bröring, M.; Köhler, S.; Link, S.; Burghaus, O.; Pietzonka, C.; Kelm, H.; Krüger, H.-J. *Chem.—Eur. J.* **2008**, *14*, 4006. (b) Ohgo, Y.; Neya, S.; Ikeue, T.; Takahashi, M.; Takeda, M.; Funasaki, N.; Nakamura, M. *Inorg. Chem.* **2002**, *41*, 4627. (c) Fitzgerald, J. P.; Haggerty, B. S.; Rheingold, A. L.; May, L.; Brewer, G. A. *Inorg. Chem.* **1992**, *31*, 2006. (d) Kostka, K. L.; Fox, B. G.; Hendrich, M. P.; Collins, T. J.; Rickard, C. E. F.; Wright, L. J.; Münck, E. *J. Am. Chem. Soc.* **1993**, *115*, 6746. (e) Fitzgerald, J. P.; Yap, G. P. A.; Rheingold, A. L.; Brewer, C. T.; May, L.; Brewer, G. A. *J. Chem. Soc., Dalton Trans.* **1996**, 1249. (f) Fettouhi, M.; Morsy, M.; Waheed, A.; Golhen, S.; Ouahab, L.; Sutter, J.-P.; Kahn, O.; Menendez, N.; Varret, F. *Inorg. Chem.* **1999**, *38*, 4910. (g) Evans, D. R.; Reed, C. A. *J. Am. Chem. Soc.* **2000**, *122*, 4660. (h) Zakharieva, O.; Schunemann, V.; Gerdan, M.; Licoccia, S.; Cai, S.; Walker, F. A.; Trautwein, A. X. *J. Am. Chem. Soc.* **2002**, *124*, 6636. (i) Niarchos, D.; Kostikas, A.; Simopoulos, A.; Coucouvanis, D.; Piltingsrud, D.; Coffman, R. E. *J. Chem. Phys.* **1978**, *69*, 4411. (j) Keutel, H.; Kapplinger, I.; Jager, E.-G.; Grodzicki, M.; Schunemann, V.; Trautwein, A. X. *Inorg. Chem.* **1999**, *38*, 2320.

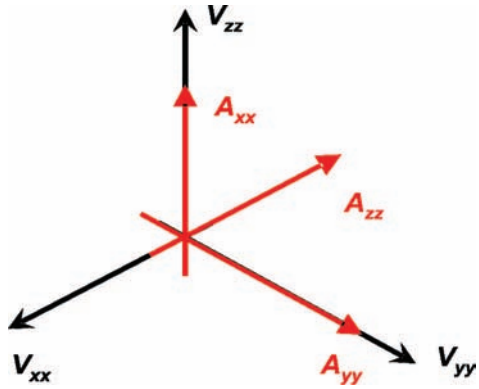

Figure 7. Orientation of the electric field gradient tensor **V** relative to the hyperfine coupling tensor **A** in **1**.

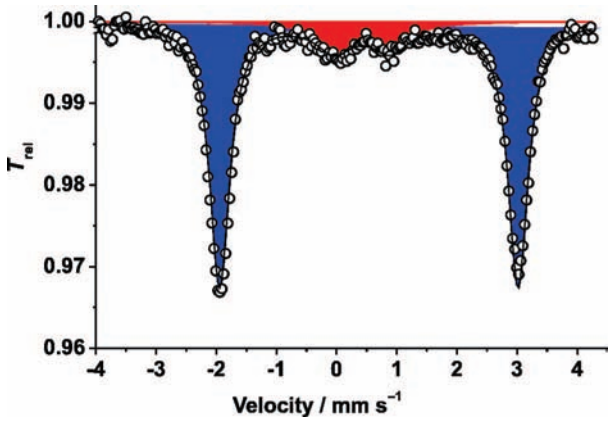

Figure 8. Zero-field ^{57}Fe Mössbauer spectrum of crystalline **2** recorded at 80 K. The solid line represents the best fit obtained with the following parameter values: (a) **2**, $\delta = 0.54$ mm s^{-1}, $|\Delta E_Q| = 4.96$ mm s^{-1}, relative intensity 84%; (b) an unidentified impurity, $\delta = 0.43$ mm s^{-1}, $|\Delta E_Q| = 0.93$ mm s^{-1}, relative intensity 16%. Color scheme: blue, **2**; red, the impurity.

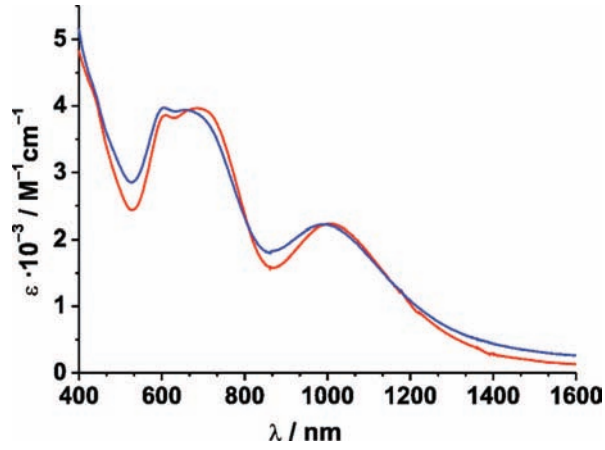

Figure 9. Electronic spectra of **1** recorded in hexane (red line) and Et_2O (blue line).

species:[44] $[Fe^{III}(^{F}pda^{2-})(^{F}dad^{\bullet-})] \rightleftarrows [Fe^{III}(^{F}pda^{\bullet-})(^{F}dad^{2-})]$. Complex **1** shows moderate solvatochromism: the hypsochromic shift of ~22 nm for the IVLLCT band is observed when the polarity of the solvent is increased in going from hexane to diethyl ether.

Besides strong absorption bands in the UV region, compound **2** shows several overlapping intense bands in the visible region.

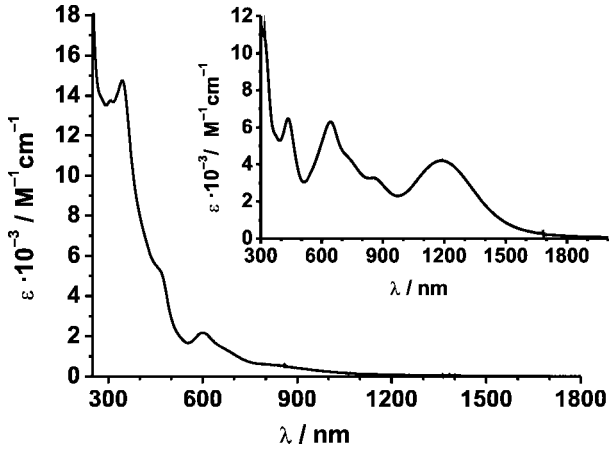

Figure 10. Electronic spectrum of **2** recorded in hexane. The electronic spectrum of **3** recorded in toluene is shown in the inset.[18]

A charge-transfer band at 600 nm is accompanied by a broad shoulder seen at 800−1000 nm. In contrast to **1**, complex **2** shows no detectable solvatochromism, as the electronic spectra of **2** recorded in hexane, toluene, and Et_2O are virtually identical.

The electronic spectrum of **3** (Figure 10 inset) has been reported to contain an intense band in the NIR region (λ_{max} = 1190 nm, $\varepsilon = 4.2 \times 10^3$ M^{-1} cm^{-1}).[18] This band has been assigned to an IVLLCT transition in the fully delocalized class-III ligand mixed-valent species: $[Fe^{III}(^{F}pda^{2-})(^{F}pda^{\bullet-})] \rightleftarrows [Fe^{III}(^{F}pda^{\bullet-})(^{F}pda^{2-})]$.[18]

e. Ground-State DFT Calculations. Full geometry optimization of **1** using the B3LYP functional[24] with van der Waals corrections[45] satisfactorily reproduced the distinctive features of the complex, including the twist angle, the $\pi-\pi$ interactions of the C_6F_5 substituents, and the intraligand bond distances (see the Supporting Information). However, the Fe−N bond distances were overestimated by 0.05−0.06 Å, which is typical for the B3LYP functional.[46] These systematic bond length overestimations lead to large deviations of the calculated and experimental values of the isomer shift. When the Mössbauer parameters were calculated using the experimental X-ray structural data, better agreement was achieved. Hence, all further calculations were performed using the X-ray structural data. Only the positions of the hydrogen atoms were optimized.

A broken-symmetry solution,[29,30] BS(3,1) $M_S = 1$, is the lowest in energy for **1**. This corresponds to an electronic structure for **1** with three α-spins located at the metal center and one β-spin distributed over the two ligands, in accordance with a triplet ground state (Figure 11). The β-spin is distributed on the NCCN backbone of the ^{F}dad ligand (−0.69) and in part (−0.31) on the ^{F}pda backbone (Figure 12). Inspection of the reduced orbital charges and orbital spin densities[19] (Table 3) yields a $(d_{x^2-y^2})^2(d_{z^2})^1(d_{yz})^1(d_{xz})^1(d_{xy})^0$ electronic configuration for the central iron ion (i.e., it is an intermediate-spin Fe^{III} ion). The singly occupied metal d_{xz} orbital is exchange-coupled to the ligand magnetic orbital, which is predominantly the ^{F}dad π^* orbital. The large orbital overlap calculated for the two magnetic orbitals, $S_{AB} = 0.56$, correlates well with a strong antiferromagnetic coupling expected for such singly occupied MOs. The effective exchange coupling constant J_{eff} ($\hat{H} = -2J\hat{\mathbf{S}}_A \cdot \hat{\mathbf{S}}_B$) estimated by the Yamaguchi equation[33] is −900

(44) Lu, C. C.; Bill, E.; Weyhermüller, T.; Bothe, E.; Wieghardt, K. *J. Am. Chem. Soc.* **2008**, *130*, 3181.

(45) (a) Grimme, S. *J. Comput. Chem.* **2004**, *25*, 1463. (b) Grimme, S. *J. Comput. Chem.* **2006**, *27*, 1787.

(46) Neese, F. *J. Biol. Inorg. Chem.* **2006**, *11*, 702.

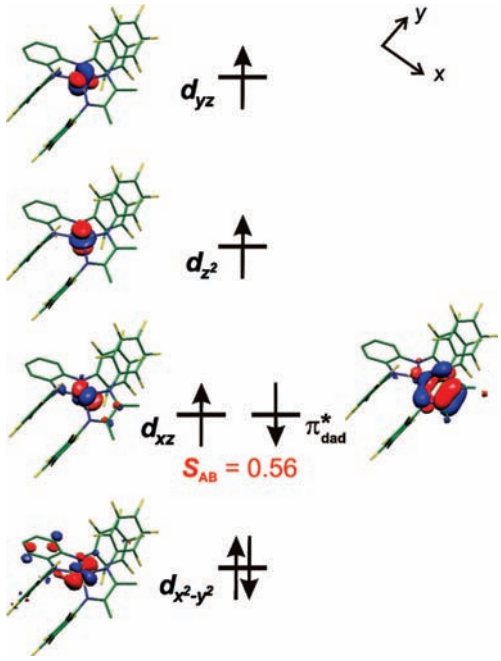

Figure 11. Qualitative MO scheme for [Fe^{III}(^{F}dad$^{\bullet-}$)(^{F}pda^{2-})] **1**.

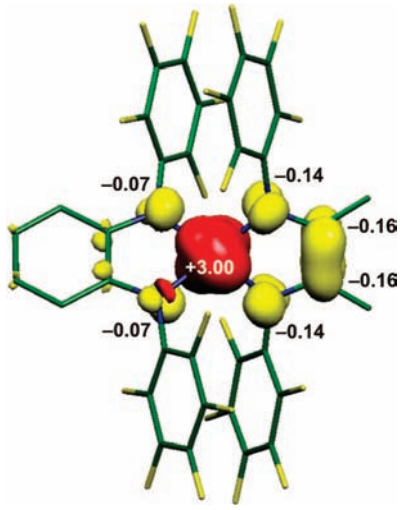

Figure 12. Broken-symmetry spin density map for [Fe^{III}(^{F}dad$^{\bullet-}$)(^{F}pda^{2-})] **1**.

cm^{-1}. This value is supported by the magnetic susceptibility measurements, which show an exclusive population of the well-isolated ground state up to 300 K.

In contrast to **1**, the lowest-energy solution found for **2** is BS(4,2) $M_S = 1$, which corresponds to four α-spins located at the iron and two β-spins located at the ligands (Figure 13). The atomic (total) spin density at the iron is +3.41, whereas the negative spin density of −1.41 is evenly dispersed over the two NCCN ligand backbones (Figure 14). Deviations from the theoretical +4.0 and −2.0 values are due to Fe−N covalent bonding and some Fe^{III} character of **2** (see the Discussion). The reduced orbital charges and orbital spin densities calculated for **2** point to the electronic configuration $(d_{x^2-y^2})^2(d_{z^2})^1(d_{yz})^1(d_{xz})^1(d_{xy})^1$, i.e., a high-spin Fe^{II} ion (Table 3). The magnetic iron orbitals d_{xz} and d_{xy} couple antiferromagnetically to two ligand-based magnetic orbitals, which are *gerade* and *ungerade* combinations of the two ligand π^* orbitals, respectively. It should be noted that the nonzero overlap $S_{AB} = 0.55$ between the metal d_{xy} orbital and the ligand π_u^* orbital results from the twisted geometry of **2** (Figure S6). For a square-planar complex, this overlap would be exactly zero. The effective coupling constant J_{eff} is estimated to be -630 cm^{-1}, which again is in agreement with the magnetic susceptibility data.

The accuracy of the electronic structures of **1** and **2** derived from the above calculations was judged by calculations of Mössbauer parameters. The calculated and experimental values are in good agreement, as shown in Table 4. The slight underestimation in the calculated values of the isomer shift might be the result of using a calibration curve based on BP86-optimized[47] iron complexes.[32] The orientation of the principal axis system of the EFG tensor of **1** is shown in Figure 15. The principal z axis is perpendicular to the least-squares plane through the four nitrogen atoms, and the principal y axis is collinear with the local C_2 axis. Complex **2** produces a similar EFG tensor at the iron center, but since V_{zz} is greater, this results in a larger quadrupole splitting constant. In fact, very similar EFG tensors were reported for high-spin ferrous and intermediate-spin ferric complexes with twisted geometries.[18] Hence, the large quadrupole splitting observed for **1** and **2** results from covalent bonding between the iron and the ligand donors, in which the valence contribution to the EFG is significantly increased rather than reduced by the covalence contribution.[18]

f. TD-DFT Calculations. Excited-state calculations on **1**−**3** at the B3LYP-TD-DFT level have been performed. Since the TD-DFT method is of limited use when applied to open-shell spin-coupled systems,[30,48] we attempted to reproduce at least qualitatively the presence of the intense NIR transition band in the electronic spectra of **1** and **3** and its absence for **2**. The results are summarized in Table 5. The full data for the first 20 excited states for **1**−**3** are provided in the Supporting Information. Surprisingly, the energy of the NIR transition in **1** and **3** is nicely reproduced in our calculations, whereas the intensities are overestimated by a factor of 2 to 3. Analysis of the Kohn−Sham orbitals (Figure 16) confirms the intervalence nature of these transitions. The charge is transferred from the filled π^*_{pda} orbital to the singly occupied π^*_{dad} orbital in **1**, whereas in **3**, virtually no charge transfer occurs because the formally filled donor π_u^* and half-filled acceptor π_g^* orbitals are fully delocalized and occupy the same space.[49] The intervalence band in **3** is more intense than that in **1** as a result of better donor/acceptor orbital overlap in **3**.

The NIR transition at 8772 cm^{-1} is also found in the calculated spectrum of **2**. Unlike the intense intervalence bands in **1** and **3**, this band represents a less intense d−d transition in **2** (Figure 17). Indeed, after the deconvolution of the experimental electronic spectrum of **2** (Figure S7 in the Supporting Information), the NIR transition is found at 10543 cm^{-1}, forming the low-energy part of the shoulder at 800−1000 nm (Figure 10).

4. Discussion

In this work, we synthesized and fully characterized the four-coordinate heteroleptic complex [Fe(^{F}dad)(^{F}pda)] **1** and the homoleptic [Fe(^{F}dad)$_2$] **2** species, whereas the related homoleptic complex [Fe(^{F}pda)$_2$] **3** has been reported previously[18] (Chart

(47) (a) Becke, A. D. *Phys. Rev. A* **1988**, *38*, 3098. (b) Perdew, J. P. *Phys. Rev. B* **1986**, *34*, 7406. (c) Perdew, J. P. *Phys. Rev. B* **1986**, *33*, 8822.
(48) Ray, K.; Weyhermüller, T.; Neese, F.; Wieghardt, K. *Inorg. Chem.* **2005**, *44*, 5345.
(49) Vogler, A.; Kunkely, H. *Comments Inorg. Chem.* **1990**, *9*, 201.

Table 3. Reduced Orbital Charges and Orbital Spin Densities Calculated for **1**−**3**^{n} Using B3LYP-DFT

	$[Fe^{III}(^Fpda^{2-})(^Fdad^{\bullet-})]$ **1**		$[Fe^{II}(^Fdad^{\bullet-})_2]$ **2**		$[Fe^{III}(^Fpda^{2-})(^Fpda^{\bullet-})]$ **3**		$[Fe^{II}(^Fpda^{2-})_2]^{2-}$ $\mathbf{3}^{2-}$		$[Fe^{III}(^Fpda^{2-})_2]^-$ $\mathbf{3}^-$	
	charge	spin	charge	spin	charge	spin	charge	spin	charge	spin
d_{z^2}	1.09	0.90	1.06	0.93	1.12[a]	0.88[a]	1.11[a]	0.88[a]	1.13[a]	0.86[a]
d_{xz}	1.28	0.68	1.22	0.76	1.28	0.66	1.18	0.86	1.32	0.73
d_{yz}	1.10	0.91	1.07	0.93	1.12	0.89	1.07	0.93	1.14	0.87
$d_{x^2-y^2}$	1.95	0.02	1.94	0.02	1.96	0.01	1.88	0.08	1.96	0.02
d_{xy}	1.06	0.39	1.21	0.66	0.99	0.28	1.25	0.78	0.93	0.19
$\sum d_i$	6.48	2.90	6.49	3.31	6.47	2.71	6.49	3.53	6.48	2.67
Fe_{total}[b]		3.00		3.41		2.82		3.62		2.75
L_{total}[c]		−1.00[d]		−1.41[d]		−0.82[d]		0.38		0.25

[a] The given populations for **3**^{n} are slightly different from these given in ref 18 because of differences in the optimized structures. Only the positions of the hydrogen atoms in this work were optimized for consistency with **1** and **2**. [b] The total spin density at the iron ion, including s and p orbitals. [c] The total spin density at the ligands. [d] Broken-symmetry solution.

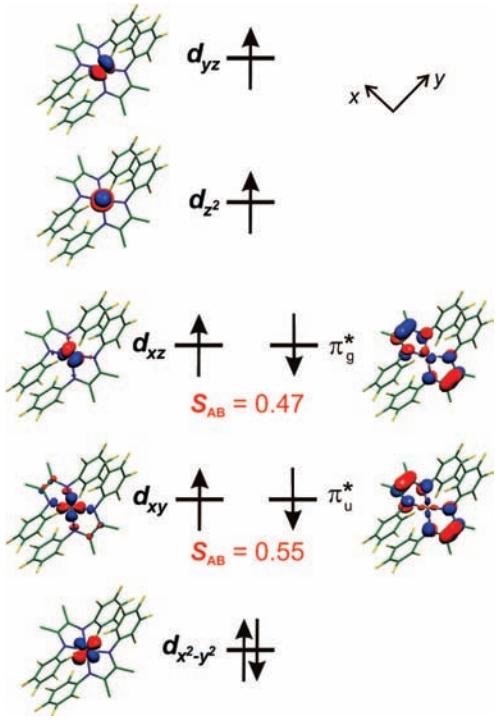

Figure 13. Qualitative MO scheme for $[Fe^{II}(^Fdad^{\bullet-})_2]$ **2**.

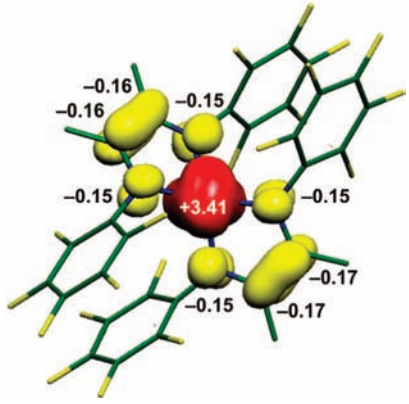

Figure 14. Broken-symmetry spin density map for $[Fe^{II}(^Fdad^{\bullet-})_2]$ **2**.

3). All three complexes possess similar twisted tetrahedral geometries of the FeN_4 polyhedron and have a triplet ground state that is the only thermally populated state at temperatures up to 290 K. However, the electronic structures of **1**−**3** are quite different.

Table 4. Mössbauer Parameters and Properties of **1** and **2** Obtained from Spin-Unrestricted B3LYP-DFT Calculations[a]

	1	**2**
δ (mm s^{-1})	+0.26 (+0.33)	+0.47 (+0.54)
ΔE_Q (mm s^{-1})	+4.40 (+4.46)	+5.04 (+4.96)
η[b]	0.4 (0.9)	0.4
ρ_{Fe}[c]	3.00	3.41
$<S^2>$[d]	2.99	3.49

[a] Experimental values are given in parentheses. [b] The asymmetry parameter: $\eta = (V_{xx} - V_{yy})/V_{zz}$, where the V_{ii} are the components of the EFG tensor. [c] The total spin density at the iron ion, including s and p orbitals. [d] The expectation value of $\hat{S}^2$, the operator for the square of the total spin.

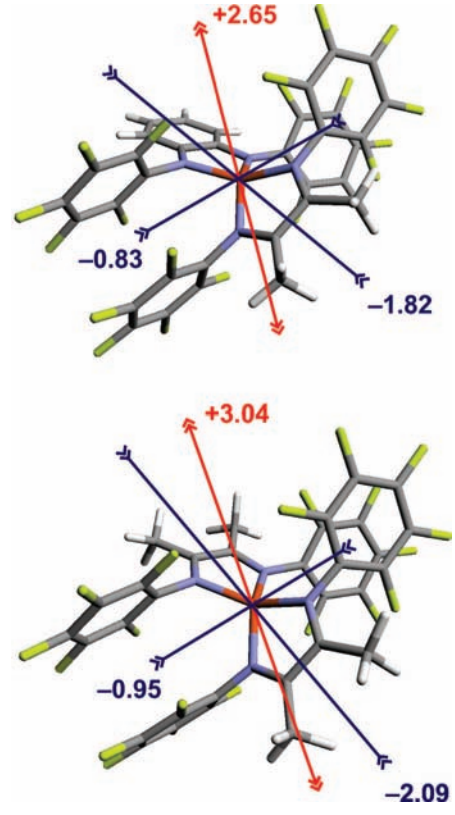

Figure 15. Orientations of the electric field gradient tensors in the molecular structures of (top) **1** and (bottom) **2** calculated using spin-unrestricted B3LYP-DFT.

a. Electronic Structure of Homoleptic Complexes 2 and 3. Complex **3** contains an intermediate-spin ferric center (S_{Fe} = $^3/_2$) with one fully reduced $^Fpda^{2-}$ ligand and one π-radical $^Fpda^{\bullet-}$ ligand (S_R = $^1/_2$) coupled antiferromagnetically to the

Table 5. NIR Transitions of **1**−**3** Calculated Using B3LYP-TD-DFT Including COSMO[a]

	1	2	3
ν (cm^{-1})	8596 (10032)	8772 (10543)	8104 (8447)
f[b]	0.054 (0.026)	0.0005 (0.0034)	0.137 (0.046)
assignment	IVLLCT	d−d	IVLLCT[d]
	$\pi^*_{pda} \rightarrow \pi^*_{dad}$	$d_{x^2-y^2} \rightarrow d_{xz}$	$\pi_u^* \rightarrow \pi_g^*$
weight[c]	0.75	0.73	0.86

[a] Numbers in parentheses are experimental values. [b] Oscillator strength. [c] The weight of the individual excitation in the state. [d] Virtually no charge transfer.[49]

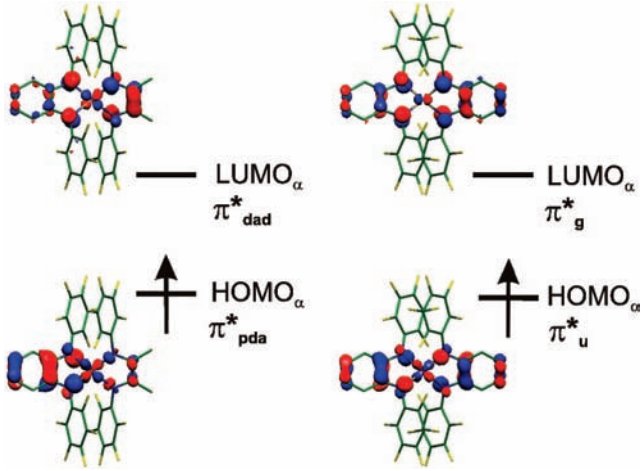

Figure 16. Donor and acceptor Kohn−Sham orbitals involved in the NIR transitions in (left) **1** and (right) **3**, obtained using spin-unrestricted B3LYP-TD-DFT calculations including COSMO.

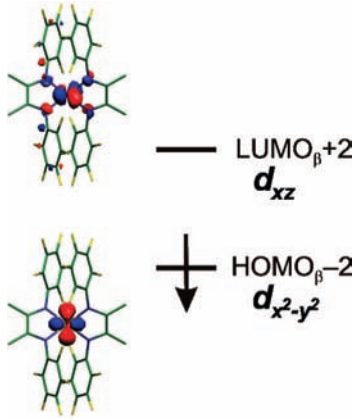

Figure 17. Donor and acceptor Kohn−Sham orbitals involved in the NIR transition in **2**, obtained using spin-unrestricted B3LYP-TD-DFT calculations including COSMO.

iron ion.[18] **3** behaves as a class-III ligand mixed-valent system, where the π radical is fully delocalized over both ligands: $[Fe^{III}(^Fpda^{2-})(^Fpda^{\bullet-})] \leftrightarrow [Fe^{III}(^Fpda^{\bullet-})(^Fpda^{2-})]$.[18]

The longer Fe−N bond distances in **2** than in **3** indicate the presence of a more reduced iron center in **2**, i.e., a high-spin ferrous ion. Additionally, the bond patterns of the NCCN ligand backbone corroborate the presence of two π-radical $^Fdad^{\bullet-}$ ligands. Hence, on the basis of X-ray crystallography, the electronic structure of **2** is $[Fe^{II}(^Fdad^{\bullet-})_2]$. This complex also possesses a triplet ground state, where a high-spin ferrous ion ($S_{Fe} = 2$) is strongly antiferromagnetically coupled to two π-radical ligands ($S_R = {}^1/_2$). The isomer shift of the high-spin Fe^{II} complex **2** is larger than that of the intermediate-spin Fe^{III} complex **3**. In fact, the Mössbauer parameters of **2** are similar to those of other high-spin Fe^{II} spin-coupled complexes.[17] It should be noted that the IVLLCT transition $[Fe^{III}(^Fpda^{2-})(^Fpda^{\bullet-})] \rightarrow [Fe^{III}(^Fpda^{\bullet-})(^Fpda^{2-})]$ in **3** is spin-allowed ($\Delta S_t = 0$), whereas the ligand-to-ligand charge transfer (LLCT) transition $[Fe^{II}(^Fdad^{\bullet-})_2] \rightarrow [Fe^{II}(^Fdad^{2-})(^Fdad^0)]$ in **2** is spin-forbidden ($\Delta S_t = 1$). Hence, the former has a very intense band in the NIR region ($\lambda_{max} = 1190$ nm, $\varepsilon = 4.2 \times 10^3$ M^{-1} cm^{-1}) that is absent in the spectrum of **2**.

The differing electronic structures of **2** and **3** are a consequence of the difference in the electron-accepting properties of the neutral ligands dad^0 and pda^0. Both ligands are members of the α-diimine ligand family, but the NCCN π-system of the dad ligand is extended by four additional phenylene carbon atoms in the pda system. The extended π conjugation should cause the LUMO of $^Fpda^0$ to be lower in energy than the LUMO of $^Fdad^0$, i.e., a negative charge is better stabilized at a pda ligand than at a dad ligand. Consequently, the two $^Fdad^0$ ligands in **2** are capable of accepting only two π electrons, leaving an Fe^{II} center. Because of the twisted tetrahedral environment, the ferrous ion adopts a high-spin state. In contrast, the two $^Fpda^0$ ligands in **3** accept three π electrons, leaving an intermediate-spin Fe^{III} center. Surprisingly, the geometric distortion in **3** is insufficient to stabilize a high-spin ferric ion but stabilizes an intermediate-spin configuration as in square-planar ferric complexes.

The spins of the two $^Fdad^{\bullet-}$ ligands in **2** are expected to interact with each other via a superexchange mechanism through the metal d orbitals. Such an interaction is strong in square-planar complexes[30] but vanishes in strictly tetrahedral complexes because there is zero overlap of the magnetic orbitals. Hence, the twisted tetrahedral complex **2** should exhibit a weaker superexchange interaction than those reported for square-planar complexes.[30] On the other hand, since the singly occupied iron d_{xz} and d_{xy} orbitals have substantial direct overlap with the singly occupied ligand π^* orbitals, strong antiferromagnetic coupling between d_{xz}/d_{xy} and the ligand π^* orbitals is anticipated. The strong antiferromagnetic ligand−metal coupling results in *parallel* alignment of the spins of the two remote ligands in the ground state. This is in stark contrast with the coupling in the low-spin d^8 square-planar complexes $[M^{II}(pda^{\bullet-})_2]$, where the antiferromagnetic superexchange through the doubly occupied d_{xz} orbital yields *antiparallel* alignment of the ligand spins in the ground state.[30]

b. Electronic Structure of Heteroleptic Complex 1. The heteroleptic complex $[Fe(^Fpda)(^Fdad)]$ **1**, containing one pda ligand and one dad ligand also possesses a twisted geometry similar to that in **2** and **3**. Furthermore, the Fe−N bond distances and Mössbauer parameters are very similar to those of **3** and confirm the presence of an intermediate-spin ferric center in **1**. Since **1** is a neutral complex with a ferric central ion, the two N,N′-coordinated ligands must carry a total of three negative charges. Thus, the electronic structure of **1** must be described as $[Fe^{III}(^Fpda^{2-})(^Fdad^{\bullet-})]$, with a monoanionic π-radical $^Fdad^{\bullet-}$ ligand, or as $[Fe^{III}(^Fpda^{\bullet-})(^Fdad^{2-})]$, with a monoanionic π-radical $^Fpda^{\bullet-}$ ligand. X-ray crystallography suggests that the unpaired electron of the π-radical anion is localized mostly on the ^Fdad fragment, with some small delocalization to the ^Fpda ligand. The DFT calculations also predict the presence of a predominantly $^Fdad^{\bullet-}$-centered π radical. The best description of the electronic structure of **1** is therefore $[Fe^{III}(^Fpda^{2-})(^Fdad^{\bullet-})]$. The triplet ground state is attained via antiferromagnetic

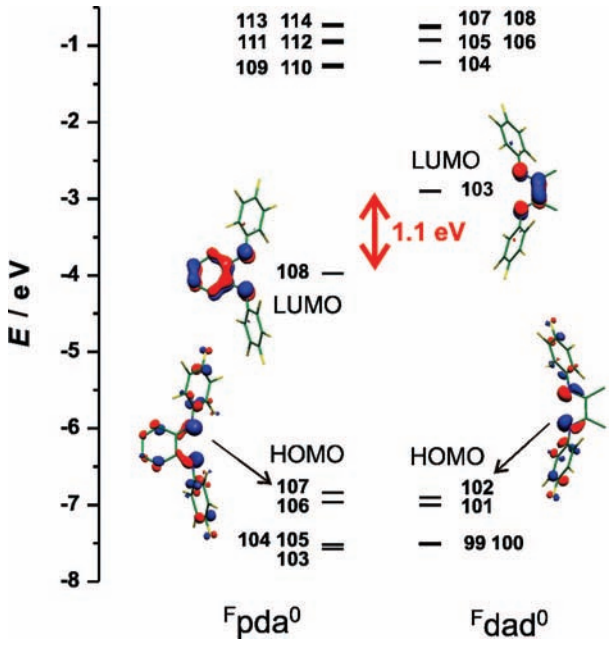

Figure 18. Kohn−Sham MOs and energy schemes for the neutral ligands (left) $^{F}pda^{0}$ and (right) $^{F}dad^{0}$ obtained from spin-unrestricted B3LYP-DFT calculations.

coupling between an intermediate-spin Fe^{III} ion ($S_{Fe} = {}^{3}/_{2}$) and the π-radical ligand $^{F}dad^{\bullet-}$ ($S_R = {}^{1}/_{2}$).

To corroborate the above notion of differing electron-accepting properties of the ligands, we performed DFT calculations on the closed-shell neutral ligands $^{F}dad^{0}$ and $^{F}pda^{0}$. The LUMO of $^{F}dad^{0}$, i.e., the redox-active π^* orbital, is found to be ~1.1 eV higher in energy than the LUMO of $^{F}pda^{0}$ (Figure 18). This calculated energy difference is in very good agreement with the energy of 1.2 eV for the IVLLCT band ($\lambda \approx 1000$ nm) observed in the electronic spectrum of **1** (Figure 9). We are aware of the fact that the calculated energy difference between the two π^* orbitals may not reflect the true thermodynamic difference between the two radical anions and therefore that the observed agreement may be somewhat fortuitous. On the other hand, the results obtained from the UV−vis−NIR spectrum of **1** and the ground-state DFT calculations on the free neutral ligands are further corroborated by the excited-state TD-DFT calculations on **1**. The position of the IVLLCT band is nicely reproduced in the TD-DFT calculations (Table 5), and the analysis of the canonical Kohn−Sham orbitals confirms the transfer of the electron density from the ^{F}pda ligand to the ^{F}dad ligand (Figure 16).

Hence, to a first approximation,[50] the $^{F}pda^{0}$ molecule is easier to reduce than the corresponding $^{F}dad^{0}$ molecule. Therefore, the π^*_{pda} orbital in **1** accommodates two electrons, yielding the fully reduced closed-shell dianion $^{F}pda^{2-}$, whereas the π^*_{dad} orbital accommodates only one electron, affording the π-radical ligand $^{F}dad^{\bullet-}$. Since the redox-active π^*_{dad} and π^*_{pda} orbitals are not orthogonal to each other, they can interact via a superexchange mechanism through the iron d_{xz} and d_{xy} orbitals, and *partial* delocalization of three π^* electrons over both ligands is expected. This is confirmed by X-ray crystallography, DFT calculations, and electronic spectroscopy. The half-width of the

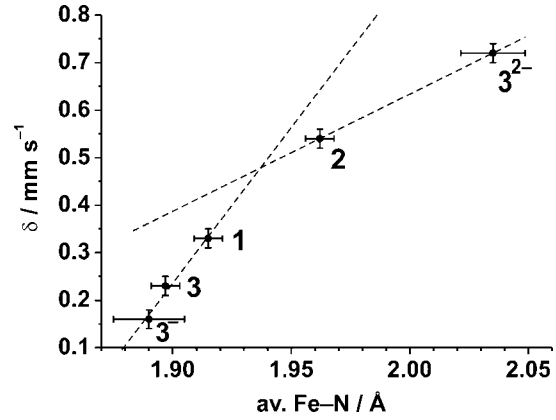

Figure 19. Correlation of the isomer shift values obtained from ^{57}Fe Mössbauer spectroscopy with the average experimental Fe−N bond distances in **1**−**3**^{n}. The dashed lines are drawn to visualize the trends within intermediate-spin ferric complexes (**3**$^{-}$, **3**, and **1**) and the high-spin ferrous complexes (**2**, **3**$^{2-}$). The error bars drawn for the average Fe−N bond distances represent 3σ values (σ = estimated standard deviation).

intense solvatochromic IVLLCT band of **1** in the NIR region calculated using the Hush equation[51] is $\Delta\nu_{calcd} = (2310\nu_{max})^{1/2} = 2200\ cm^{-1}$, which is smaller than the experimentally observed value, $\Delta\nu_{exp} = 3040\ cm^{-1}$. Thus, **1** behaves as a class-II ligand mixed-valent system.

c. Ambiguity of the Electronic Structures of 1−3. On the basis of the above discussion, the electronic structure of **1** is a localized class-II mixed-valent [$Fe^{III}(^{F}pda^{2-})(^{F}dad^{\bullet-})$] system, in which an intermediate-spin Fe^{III} ion is antiferromagnetically coupled to one π-radical $^{F}dad^{\bullet-}$ ligand. The electronic structure of **2** is best described as [$Fe^{II}(^{F}dad^{\bullet-})_2$], in which a high-spin Fe^{II} ion is antiferromagnetically coupled to two π-radical $^{F}dad^{\bullet-}$ ligands. Finally, the electronic structure of **3** was formulated[18] as a fully delocalized class-III mixed-valent [$Fe^{III}(^{F}pda^{2-})(^{F}pda^{\bullet-})$] system, where an intermediate-spin Fe^{III} ion is antiferromagnetically coupled to one π-radical $^{F}pda^{\bullet-}$ ligand.

It is now very instructive to compare the average Fe−N bond distances and the isomer shifts in the spin-coupled complexes **1**−**3** and two closely related complexes, namely, [$Fe^{II}(^{F}pda^{2-})_2]^{2-}$ (**3**$^{2-}$), i.e., a dianion with a high-spin Fe^{II} center and two closed-shell dianionic ligands, and [$Fe^{III}(^{F}pda^{2-})_2]^{-}$ (**3**$^{-}$), i.e., a monoanion with an intermediate-spin Fe^{III} ion and two closed-shell dianionic ligands.[18] Complexes **3**$^{2-}$ and **3**$^{-}$ possess $S_t = 2$ and $S_t = {}^{3}/_{2}$ ground states, respectively. It should be noted that **3**$^{2-}$ and **3**$^{-}$ are classical Werner-type complexes with unambiguously determined oxidation states of the iron ions and closed-shell diamagnetic ligands $^{F}pda^{2-}$. The twisted geometries of the FeN_4 polyhedra in **1**−**3**^{n} (i.e., **1**−**3**, **3**$^{-}$, and **3**$^{2-}$) are very similar.

It is observed that the isomer shift increases in the order **3**$^{-}$, **3**, **1**, **2**, **3**$^{2-}$, which correlates nicely with the increasing average Fe−N distance (Figure 19). The intermediate-spin ferric complexes **1**, **3**, and **3**$^{-}$ show the typical short average Fe−N bond distances (1.89−1.92 Å), in contrast to the high-spin ferrous complexes **2** and **3**$^{2-}$, which possess typical longer average Fe−N bond distances in the range 1.96−2.03 Å. The isomer shifts of the intermediate-spin ferric complexes **1**, **3**, **3**$^{-}$, which fall in the range 0.15−0.33 mm s^{-1}, are lower than those of the high-spin ferrous complexes **2** and **3**$^{2-}$, observed at 0.54−0.75 mm s^{-1}.

(50) Bond, A. M. In *Comprehensive Coordination Chemistry II*; McCleverty, J. A., Meyer, T. J., Eds.; Elsevier: Oxford, U.K., 2004; Vol. 2, p 197.

(51) Hush, N. S. *Prog. Inorg. Chem.* **1967**, *8*, 391.

The observed diversity of isomer shift values and average Fe−N distances within the two subseries can be rationalized by consideration of the different donor−acceptor abilities of the ligands. The two $^{F}dad^{\bullet-}$ radical ligands in **2** are clearly much stronger π acceptors but much weaker σ/π donors than the two fully reduced $^{F}pda^{2-}$ ligands in $\mathbf{3}^{2-}$, which results in the shorter average Fe−N distances and the smaller isomer shift in **2**. It should be noted that the d_{xy} and d_{xz} iron orbitals can be used for π back-bonding in **2**. The electronic structure of **1** can then be viewed as an example of an extremely strong π back-donation in which almost complete intramolecular Fe → L electron transfer has occurred, yielding a ferric complex with an unoccupied d_{xy} orbital and a reduced $^{F}pda^{2-}$ ligand. Thus, one could envisage a compound in which exactly half of a negative charge is transferred from the iron to the ligand, rendering the assignment of an integer physical oxidation state meaningless. As can be estimated from the intersection of the two lines in Figure 19, such a complex would have an isomer shift of ∼0.47 mm s^{-1} and an average Fe−N distance of ∼1.94 Å.

Thus, complexes $\mathbf{3}^{-}$ and $\mathbf{3}^{2-}$ located at the extremes in Figure 19 represent the typical "pure" examples of intermediate-spin Fe^{III} and high-spin Fe^{II} species, respectively. However, the description of the electronic structures of spin-coupled **1** and **2**, which are located closer to the point of uncertainty (1.94 Å, 0.47 mm s^{-1}) in Figure 19 is less straightforward. Indeed, the Fe−N bond distance of 1.962(2) Å in **2** is surprisingly short[17,18,20,37,52] and the observed 0.54 mm s^{-1} isomer shift of the quadrupole doublet rather small[18,20] for a typical four-coordinate tetrahedral high-spin ferrous complex. Hence, we performed a more detailed investigation of the electronic structures of $\mathbf{1}-\mathbf{3}^{n}$ using DFT calculations.

d. Probing of the Electronic Structures by DFT Calculations. Oxidation and spin states of the metal ion and the ligands can be probed by analysis of the MOs and spin densities (recent examples from our group are collected in refs 16, 17, 44, and 53). The analysis of highly delocalized canonical orbitals is problematic for open-shell and highly covalent systems. In such cases, canonical orbitals are transformed into other types of more localized orbitals. Sometimes several different types of orbitals are simultaneously used to build qualitative MO schemes for spin-coupled systems. For example, two types of orbitals were used in this work to generate qualitative MO schemes: corresponding orbitals[31] were used to visualize spin-coupled pairs, while the rest were quasi-restricted orbitals.[54] It is not surprising that simultaneous analysis of several types of orbitals and the process of choosing those that constitute a qualitative MO scheme might be complicated and could result in an erroneous description of the electronic structure.

Another method of examining the electronic structure is the analysis of calculated spin densities.[16,17,44,53] This is quite straightforward and involves reporting the atomic (total) spin density at the metal, which gives its oxidation and spin state, and the spin densities at the ligands, which, in combination with an assessment of intraligand bond distances,[4,7,55] yield the oxidation level of the ligands. However, as mentioned previously,[18] investigation of the electronic structure by relying on the atomic spin densities can be inaccurate because of covalency and spin polarization effects. For instance, an atomic spin density of 5.0 would be expected for a high-spin d^5 ion because of its five unpaired electrons, but if strongly donating ligands are present, the spin density of each metal d orbital may decrease by, let us say, 20%, leaving 0.8 spins per d orbital. Thus, the summation over all of the d orbitals would give an atomic spin density of 4.0, which one could mistakenly attribute to a high-spin d^6 ion.[56] However, careful analysis of the spin density *per d orbital* can eliminate such errors.

e. Analysis of Reduced Orbital Populations of 1−3 and Related Complexes. Reduced orbital charges and spin densities calculated for $\mathbf{1}-\mathbf{3}^{n}$ are shown in Table 3. The total *charge* population at iron d orbitals is nearly constant for $\mathbf{1}-\mathbf{3}^{n}$ in the range 6.47−6.49 electrons, resulting from enhanced covalency of the FeN_4 unit. The *spin* population, for molecules not having a singlet spin state, is much more informative. The intermediate-spin d^5 complexes **1**, **3**, and $\mathbf{3}^{-}$ show 2.67−2.90 spins at the iron d orbitals, which is significantly less than the 3.31−3.53 spins observed for the high-spin d^6 complexes **2** and $\mathbf{3}^{2-}$. The calculated spin populations are lower than the ideal values of 3.0 and 4.0 for intermediate-spin d^5 and high-spin d^6 ions, respectively.

The orbital charges and spin densities of d_{z^2}, d_{yz}, and $d_{x^2-y^2}$ in $\mathbf{1}-\mathbf{3}^{n}$ are very similar. At the d_{z^2} and d_{yz} orbitals, ∼1.0 electrons and ∼1.0 spins are found, which is a clear indication that these orbitals are formally half-occupied. In contrast, ∼2.0 charges and ∼0.0 spins are located at the $d_{x^2-y^2}$ orbital, pointing to the presence of a doubly occupied metal d orbital. The charge population at the d_{xz} orbital in $\mathbf{1}-\mathbf{3}^{n}$ increases to 1.18−1.32 electrons, while the spin population decreases to 0.66−0.86, which results from an extended overlap of the d_{xz} orbital with a half- or fully occupied ligand π^* orbital. Thus, the d_{xz} orbital in $\mathbf{1}-\mathbf{3}^{n}$ is formally singly occupied. It is therefore interesting that the population of the d_{xy} orbital in $\mathbf{1}-\mathbf{3}^{n}$ varies considerably. It should be noted that its occupancy ultimately determines the difference between a high-spin ferrous d^6 ion (singly occupied d_{xy}) and an intermediate-spin ferric d^5 ion (unoccupied d_{xy}). The charge population of the d_{xy} orbital in $\mathbf{1}-\mathbf{3}^{n}$ allows us to tentatively divide these complexes into two groups. The first group consists of **1**, **3**, and $\mathbf{3}^{-}$, all of which show relatively low d_{xy} charge populations of 0.93−1.06. The second group, consisting of **2** and $\mathbf{3}^{2-}$, shows larger d_{xy} charge populations of 1.21−1.25. In addition, the spin population of the d_{xy} orbital varies considerably, from the smallest value of 0.19 in $\mathbf{3}^{-}$ to the largest value of 0.78 in $\mathbf{3}^{2-}$. Thus, the d_{xy} orbital is formally empty in $\mathbf{3}^{-}$, resulting in an intermediate-spin d^5 ion, but singly occupied in $\mathbf{3}^{2-}$, giving rise to a high-spin d^6 ion.

(52) (a) Gibson, V. C.; O'Reilly, R. K.; Reed, W.; Wass, D. F.; White, A. J. P.; Williams, D. J. *Chem. Commun.* **2002**, 1850. (b) Kervern, G.; Pintacuda, G.; Zhang, Y.; Oldfield, E.; Roukoss, C.; Kuntz, E.; Herdtweck, E.; Basset, J. M.; Cadars, S.; Lesage, A.; Coperet, C.; Emsley, L. *J. Am. Chem. Soc.* **2006**, *128*, 13545. (c) Bart, S. C.; Hawrelak, E. J.; Schmisseur, A. K.; Lobkovsky, E.; Chirik, P. J. *Organometallics* **2004**, *23*, 237. (d) Breuer, J.; Fruhauf, H. W.; Smeets, W. J. J.; Spek, A. L. *Inorg. Chim. Acta* **1999**, *291*, 438.

(53) (a) Lu, C. C.; Bill, E.; Weyhermüller, T.; Bothe, E.; Wieghardt, K. *Inorg. Chem.* **2007**, *46*, 7880. (b) Kokatam, S.; Ray, K.; Pap, J.; Bill, E.; Geiger, W. E.; LeSuer, R. J.; Rieger, P. H.; Weyhermüller, T.; Neese, F.; Wieghardt, K. *Inorg. Chem.* **2007**, *46*, 1100. (c) Kapre, R. R.; Bothe, E.; Weyhermüller, T.; DeBeer George, S.; Muresan, N.; Wieghardt, K. *Inorg. Chem.* **2007**, *46*, 7827. (d) Chlopek, K.; Muresan, N.; Neese, F.; Wieghardt, K. *Chem.—Eur. J.* **2007**, *13*, 8390.

(54) Neese, F. *J. Am. Chem. Soc.* **2006**, *128*, 10213.

(55) (a) Chaudhuri, P.; Verani, C. N.; Bill, E.; Bothe, E.; Weyhermüller, T.; Wieghardt, K. *J. Am. Chem. Soc.* **2001**, *123*, 2213. (b) Bhattacharya, S.; Gupta, P.; Basuli, F.; Pierpont, C. G. *Inorg. Chem.* **2002**, *41*, 5810.

(56) Spikes, G. H.; Bill, E.; Weyhermüller, T.; Wieghardt, K. *Angew. Chem., Int. Ed.* **2008**, *47*, 2973.

(57) Bencini, A.; Gatteschi, D. *Electron Paramagnetic Resonance of Exchange Coupled Systems*; Springer-Verlag: Berlin Heidelberg, 1990; p 48.

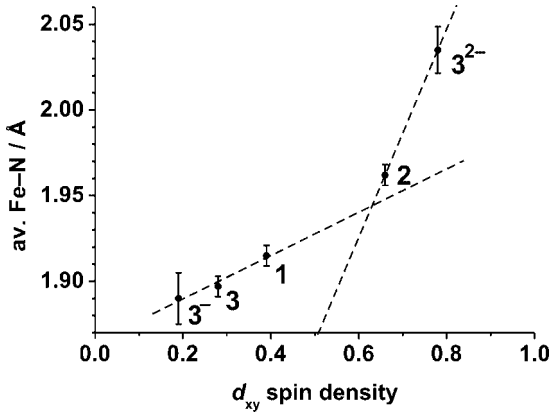

Figure 20. Correlation of the experimental average Fe−N bond distance with the calculated d_{xy} spin density (obtained using spin-unrestricted B3LYP-DFT) in **1**−**3**^{n}. The dashed lines are drawn to visualize the trends within intermediate ferric compounds ($\mathbf{3}^-$, **3**, and **1**) and high-spin ferrous complexes (**2** and $\mathbf{3}^{2-}$). The error bars drawn for the average Fe−N bond distances represent 3σ values.

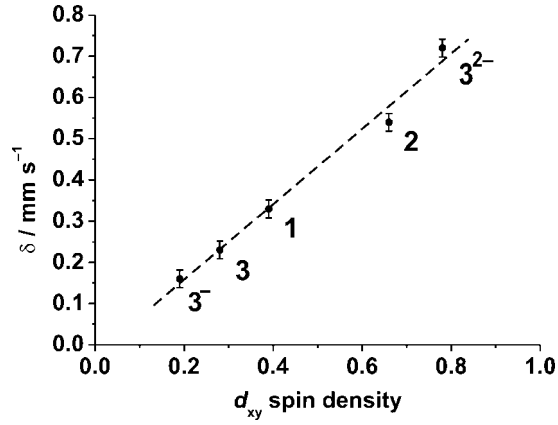

Figure 21. Correlation of the isomer shift in the experimental ^{57}Fe Mössbauer spectra with the calculated d_{xy} spin density (obtained using spin-unrestricted B3LYP-DFT) in **1**−**3**^{n}. The dashed line is drawn to visualize the observed trend.

The spin populations at the d_{xy} orbital in **1**−**3** have values that clearly are intermediate between those in the $\mathbf{3}^-$ and $\mathbf{3}^{2-}$ complexes. It can be argued that if the spin population at the d_{xy} orbital is less than 0.5, then it is formally empty, which corresponds to an intermediate-spin d^5 ion. Conversely, if the spin population at the d_{xy} orbital exceeds 0.5, the orbital is formally singly occupied, and the complex possesses a high-spin d^6 ion. Unfortunately, there is no clearly defined borderline between these two extremes. Therefore, the assignment of a spectroscopic oxidation state at the metal is somewhat arbitrary.

Keeping in mind the fact that the electronic structures of **1**−**3** fill the continuum between the two extremes of a high-spin Fe^{II} ion coordinated to two radical monoanions and an intermediate-spin Fe^{III} ion coordinated to one radical monoanion and one closed-shell dianion, we assign integer oxidation states in **1**−**3**, as commonly preferred by coordination chemists. Thus, complex **3**, with a spin population at the d_{xy} orbital of 0.28, is best described as an intermediate-spin Fe^{III} complex[18] $[Fe^{III}(^{F}pda^{2-})(^{F}pda^{\bullet-})]$ with some high-spin Fe^{II} (i.e., $[Fe^{II}(^{F}pda^{\bullet-})_2]$) character. Complex **1**, which is also assigned as an intermediate-spin Fe^{III} complex $[Fe^{III}(^{F}pda^{2-})(^{F}dad^{\bullet-})]$, exhibits even higher degree of high-spin Fe^{II} (i.e., $[Fe^{II}(^{F}pda^{\bullet-})(^{F}dad^{\bullet-})]$) character due to the d_{xy} spin population of 0.39. Finally, **2** is assigned as a high-spin Fe^{II} complex $[Fe^{II}(^{F}dad^{\bullet-})_2]$ with some intermediate-spin Fe^{III} (i.e., $[Fe^{III}(^{F}dad^{2-})(^{F}dad^{\bullet-})]$) contribution, as confirmed by the d_{xy} spin population of 0.66.

It should be noted that the minor contributions to the electronic structures in **1**−**3** are important, as they provide a nice explanation of the experimental data. The smooth increase of the d_{xy} spin population (i.e., the increase in Fe^{II} character) in the order $\mathbf{3}^-$, **3**, **1**, **2**, $\mathbf{3}^{2-}$ correlates well with the increasing Fe−N bond distances in the series (Figure 20). In the Mössbauer spectra, the smallest isomer shift (in the ferric complex $\mathbf{3}^-$) increases to the largest one (in the ferrous species $\mathbf{3}^{2-}$) in the same order. In fact, a nearly linear correlation between the isomer shift and the spin population at the d_{xy} orbital is observed (Figure 21).

5. Conclusions

The heteroleptic complex $[Fe^{III}(^{F}pda^{2-})(^{F}dad^{\bullet-})]$ **1** containing both pda and dad ligands was synthesized and fully characterized. The electronic structure of **1** is significantly different from the electronic structure of the homoleptic complex $[Fe^{II}(^{F}dad^{\bullet-})_2]$ **2** and that of the homoleptic species $[Fe^{III}(^{F}pda^{2-})(^{F}pda^{\bullet-})]$ **3** described previously. Since the redox-active LUMO of $^{F}pda^{0}$ is ~1.1 eV lower in energy than the LUMO of $^{F}dad^{0}$, the ^{F}pda ligand is a better electron acceptor than its ^{F}dad analogue. This results in different spin density distributions in **1**−**3**, in spite of the fact that all three complexes possess a triplet ground state. The electronic structures of **1**−**3** are best described as follows: **1** is a class-II ligand mixed-valent complex containing an intermediate-spin Fe^{III} center ($S_{Fe} = {}^3/_2$) antiferromagnetically coupled to a π-radical $^{F}dad^{\bullet-}$ ligand. Complex **2** possesses a high-spin Fe^{II} ion ($S_{Fe} = 2$) that is antiferromagnetically coupled to two π-radical $^{F}dad^{\bullet-}$ ligands. Finally, **3** was described as a class-III ligand mixed-valent species containing an intermediate-spin Fe^{III} ion ($S_{Fe} = {}^3/_2$) antiferromagnetically coupled to a π-radical $^{F}pda^{\bullet-}$ ligand. Thus, we elucidated how the oxidation and spin states of the iron ions, the oxidation levels of the ligands, and the degree of delocalization of unpaired electron density on the ligands vary in spin-coupled **1**−**3**.

The detailed examination of the electronic structures by analysis of the reduced orbital charges and spin densities obtained from the B3LYP-DFT calculations suggests some ambiguity in determination of the oxidation states in **1**−**3**. In fact, the electronic structures of **1**−**3** may be described as a continuum between the two extremes of a high-spin Fe^{II} ion $(d_{x^2-y^2})^2(d_{z^2})^1(d_{yz})^1(d_{xz})^1(d_{xy})^1$ coordinated to two radical monoanions and an intermediate-spin Fe^{III} ion $(d_{x^2-y^2})^2(d_{z^2})^1(d_{yz})^1(d_{xz})^1(d_{xy})^0$ coordinated to one radical monoanion and one closed-shell dianion. The varying occupancy of the iron d_{xy} orbital produces the continuum of electronic structures in **1**−**3**. Thus, the ferric complexes **1** and **3** acquire some Fe^{II} character while the ferrous complex **2** acquires some Fe^{III} character. The increasing spin density at the d_{xy} orbital in the series **3**, **1**, **2** (i.e., the increase in high-spin Fe^{II} character and decrease in intermediate-spin Fe^{III} character) results in the observed elongation of the Fe−N bond distances and the increase of the isomer shift in the ^{57}Fe Mössbauer spectra.

The analysis of reduced orbital charges and spin densities is a useful method for the investigation and illustration of the electronic configuration in transition-metal complexes, including difficult cases of spin-coupled systems with high degrees of ligand−metal covalency.

Acknowledgment. Prof. Dr. Frank Neese and Dr. Taras Petrenko (Universität Bonn, Germany) are acknowledged for their

fruitful advice concerning the DFT calculations. Andreas Göbels, Heike Schucht, and Bernd Mienert are thanked for measurements. M.M.K. is grateful to the Max Planck Society for a postdoctoral fellowship.

Supporting Information Available: Illustrations of a twisted tetrahedral geometry and a $\pi-\pi$ stacking structure, alternative fits of the SQUID and Mössbauer spectra, and the fully optimized geometry for **1**; MOs and the deconvolution of the electronic spectrum for **2**; results of excited-state calculations and population analyses for **1**−**3**; and crystallographic data for **1** and **2**. This material is available free of charge via the Internet at http://pubs.acs.org.

JA808149K